Attanayake, J., Sandiford, D., Schleicher, L. S., Jones, A., Gibson, G., Sandiford, M. (2019): Interacting Intraplate Fault Systems in Australia: The 2012 Thorpdale, Victoria, Seismic Sequences. - *Journal of Geophysical Research*, *124*, 5, pp. 4673—4693.

DOI: http://doi.org/10.1029/2018JB016945

JGR Solid Earth

RESEARCH ARTICLE
10.1029/2018JB016945

Interacting Intraplate Fault Systems in Australia: The 2012 Thorpdale, Victoria, Seismic Sequences

Januka Attanayake[1], Dan Sandiford[1,2], Lisa S. Schleicher[3], Abraham Jones[1], Gary Gibson[1], and Mike Sandiford[1]

[1]The School of Earth Sciences, University of Melbourne, Parkville, Victoria, Australia, [2]Now at GFZ, Potsdam, Germany, [3]Rockville, MD, USA

Key Points:
- The two largest earthquakes (M_w 4.9 and 4.3) in the seismic sequence indicate thrust faulting in southeast Australia
- Higher than average stress drop (57 and 28 MPa) suggests the rupture of strong faults with longer recurrence intervals
- Adjacent fault planes ruptured, implying fault interaction through interplay between stress conditions and fluid diffusion

Supporting Information:
- Supporting Information S1

Correspondence to:
J. Attanayake,
januka.attanayake@unimelb.edu.au

Citation:
Attanayake, J., Sandiford, D., Schleicher, L. S., Jones, A., Gibson, G., & Sandiford, M. (2019). Interacting intraplate fault systems in Australia: The 2012 Thorpdale, Victoria, seismic sequences. *Journal of Geophysical Research: Solid Earth*, *124*. https://doi.org/10.1029/2018JB016945

Received 28 OCT 2018
Accepted 26 MAR 2019
Accepted article online 4 APR 2019

Abstract Using a new seismic waveform data set, we locate 234 earthquakes and estimate source parameters (focal mechanisms, magnitude, and stress drop) of the two largest earthquakes (E1 and E2) in the 2012 seismic sequence in Thorpdale, Victoria. The focal mechanisms suggest thrust faulting, consistent with previous observations in southeast Australia. The estimated magnitudes are M_w 4.9 ± 0.14 (E1) and 4.3 ± 0.1 (E2). The estimates of stress drop 57 ± 7.4 MPa (E1) and 28 ± 2.4 MPa (E2) reflect strength of faults in an intraplate environment. By analyzing spatiotemporal distribution of aftershocks, we show that E1 and E2 reflect two separate seismic sequences about a month apart. E1 and E2 ruptured two adjacent faults with orientations 218°/78°/78° (Fault 1) and 134°/27°/171° (Fault 2), respectively, where angles indicate strike/dip/slip rake. To test causal mechanism of fault interaction, we performed Coulomb stress modeling, which shows very weak unloading of E2 by E1. Thus, we infer that fault interaction might instead reflect remotely triggered fluid diffusion. Also, a local rotation of the stress field proceeding E1 might have favorably reoriented Fault 2 for failure. Finally, we identify an apparent correlation between high heat flow and seismicity in southeastern Australia, suggesting a combination of mechanisms including transient stress perturbations and lithospheric thermal weakening associated with high heat flow as the principal factors localizing intraplate seismicity.

Plain Language Summary The 2012 earthquake sequence in Thorpdale is the most recent and significant seismic activity in southeast Australia, during which two moderate-sized earthquakes were felt in the region with the second earthquake thought to be an aftershock of the first. Using a newly assembled data set, we estimate source parameters of these earthquakes and locate 232 smaller earthquakes associated with this seismic sequence. In this study, we show that faults ruptured with thrust motion, the moment magnitude of the two largest earthquakes are 4.9 and 4.3, and the stress release per fault length (57 and 28 MPa) is larger than the global average. By locating aftershocks, we also show that the two largest earthquakes ruptured two separate faults rather than one. The absence of any plausible Coulomb stress loading suggests that these different faults interacted with each other through other mechanisms such as a fluid diffusion.

1. Introduction

A rare intraplate earthquake shook the residents of Thorpdale in Southeast Australia on 19 June 2012 at 10:53:29 UTC (henceforth E1). A month later, on 20 July 2012, another significant earthquake struck approximately the same region at 09:11:31 UTC (henceforth E2), which was initially thought to be an aftershock of E1. The preliminary magnitude and hypocentral depth assigned in the U.S. Geological Survey catalog to these two earthquakes, respectively, are m_b 5.2 and 10 km and m_b 4.6 and 13 km with a hypocentral separation of ~5 km (Figure 1). Being a sparsely populated small town, Thorpdale suffered only modest losses from these shocks (AUD ~20 M; Calligeros, 2014). However, the 1989 M_w 5.4 earthquake in Newcastle, NSW, that claimed 13 lives, injured 160 people, and incurred ~AUD 4B of economic losses (2008 Year Book Australia, Australian Bureau of Statistics) exemplifies the impact that an earthquake similar in size to E1 can cause if it were to hit a major population center. Note that the Central Business District of Melbourne is located just ~120 km northwest of the Thorpdale earthquakes. Table 1 documents source parameters of the largest earthquakes to strike this region in the last 53 years.

In Southeastern Australia, deformation is slow with strain rates estimated to be less than 10^{-9} year^{-1} (Sandiford et al., 2004). The maximum horizontal compressive stress (S_{Hmax}) in this region is NW-SE

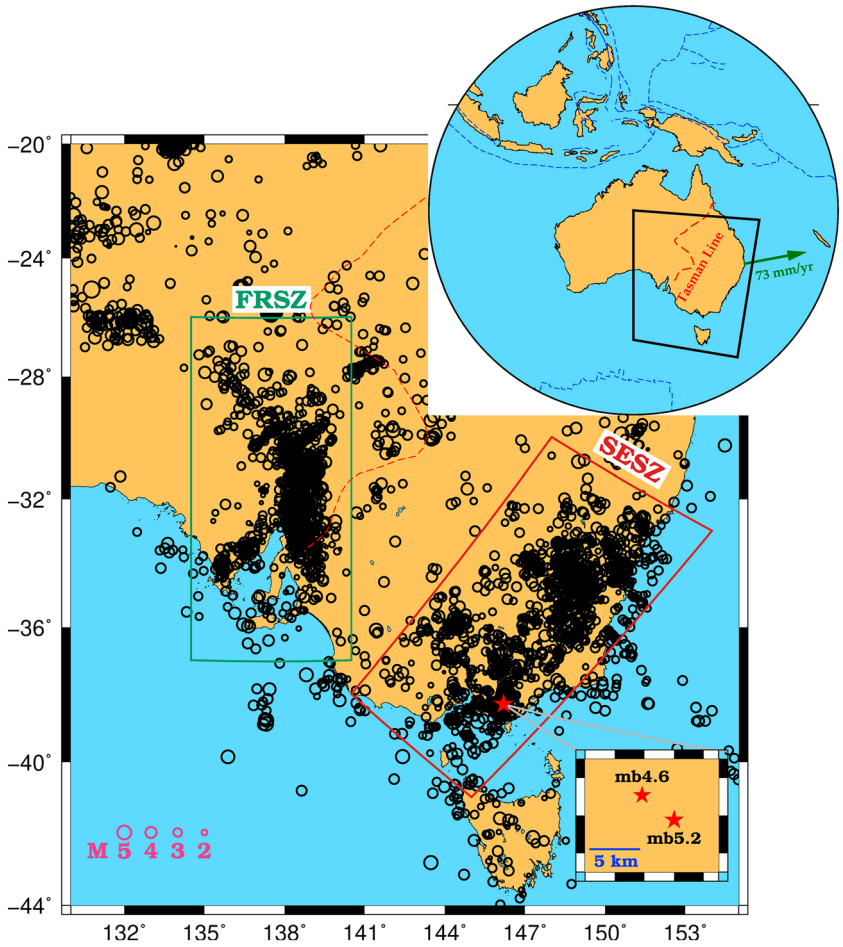

Figure 1. Seismicity of south and southeastern Australia since 1967 from IRIS Wilber 3 (https://ds.iris.edu/wilber3/find_earthquake). Seismicity in this region is localized in two regions: Southeastern Seismic Zone (SESZ) and Flinders Range Seismic Zone (FRSZ). Open circles show the location of earthquakes with their radii scaled to magnitude. The 2012 Thorpdale earthquake sequence (red star) is located within SESZ, and the inset shows the U.S. Geological Survey locations of the two largest earthquakes along with their preliminary magnitudes. The Tasman line generally divides Precambrian cratons to the west from younger Paleozoic rocks to the east. The Australian continent is moving toward the northeast at ~70 mm/year with respect to the Pacific plate.

oriented (Nelson et al., 2006; Rajabi et al., 2017), which is mainly controlled by far-field tectonic forces generated at the Indo-Australian-Eurasian-Pacific plate collision zones with local sources introducing secondary heterogeneity (Coblentz et al., 1995, 1998; Heidbach et al., 2007; Zhao & Müller, 2001). The accumulated stress due to this slow deformation is released primarily in the Southeastern Seismic Zone and the Flinders Range Seismic Zone (Figure 1), where tentative predictions of shortening can be up to 250 m/Ma (Célérier et al., 2005; Sandiford, 2003; Sandiford & Quigley, 2009). In this study, we focus on

Table 1
Source Parameters of Earthquakes Recorded in the Region Since 1967

Date	Location	Magnitude	Latitude	Longitude	Depth (km)	Reference
03/05/1966	Mount Hotham	M_L 5.5	−37.042	147.158	15	1
22/06/1969	Boolarra	M_L 5.0	−38.540	146.340	0	2
21/11/1982	Wonnangatta	M_L 5.4	−37.205	146.956	17	1
25/09/1996	Thomson Dam	M_L 5.0	−37.880	146.430	11	1
29/08/2000	Boolarra	M_L 5.0	−38.420	146.290	18	1
19/06/2012	Thorpdale	m_b 5.2	−38.304	146.200	10	3

Note. References: 1 = Leonard et al. (2002); 2 = Geoscience Australia catalog; 3 = U.S. Geological Survey catalog. Dates are formatted as DD/MM/YYYY.)

the 2012 seismic sequence in Thorpdale—the most recent and significant seismic activity in the Southeastern Seismic Zone.

A critical step in mitigating hazard from earthquakes similar to the Thorpdale earthquakes is understanding the origin of fault rupture in intraplate settings. The physics that governs the origin of such earthquakes, however, is still not well understood (Calais et al., 2005). Recent evidence points to a process where intraplate fault systems located tens to hundreds of kilometers apart interact with each other over many hundreds of years to produce large earthquakes (Liu et al., 2011, 2014), of which precise knowledge is still missing. The episodic activation and long quiescence (>10,000 years) of individual faults as observed in Australia from paleoseismic studies further confounds analyzing intraplate earthquakes (Clark & McCue, 2003; Crone et al., 2003). This latter fact is used for justifying space-for-time substitution adopted in the study of stable continental earthquakes (Johnston & Kanter, 1990). The inevitable catastrophic nature of these earthquakes (England & Jackson, 2011), albeit low probability, together with the utility of space-for-time substitution and yet to be validated self-similarity hypothesis (Prieto et al., 2004; Shearer, 2012), rationalizes studying the physics of intraplate earthquakes regardless of their magnitude.

In this study, we relocate and estimate source parameters of E1 and E2 using a newly assembled seismic data set. The use of seismic stations close to the fault ruptures (<850 km) from a temporary open network and a private network that records waves in a wide frequency band allows us to improve the precision of parameters estimated, which is important for analyzing seismic hazard accurately and understanding the physics of rupture. In addition to E1 and E2, we locate 232 aftershocks with $M_L \leq 3.4$ in the area, combine our results with available geologic information to identify the fault planes, and discuss their geodynamic implications to the region. We explore whether E2 resulted from migration of seismicity to an adjacent fault due to static stress transfer following E1. The magnitude difference (0.6 units) between E1 and E2 is less than the 1.2 magnitude units generally required to be classified as an aftershock (Båth, 1965; Shcherbakov & Turcotte, 2004), which also suggests that E2 is a separate earthquake possibly triggered by E1.

2. Methods

2.1. Hypocenters of Earthquakes

We locate earthquakes using eqFocus program (es&s, 2010), proprietary software used for locating earthquakes by the Seismology Research Centre. This program solves the location problem using a nonlinear least squares procedure (Levenberg, 1944; Marquardt, 1963). Prior to becoming proprietary, it has been used to locate earthquakes in Australia (Gibson et al., 1981). We also located earthquakes with the program HYP (Lienert & Havskov, 1995) as implemented in SEISAN (Havskov & Ottemoller, 1999) and confirmed that the locations obtained by the two methods differ by only <2 km on average, which is also the average location uncertainty estimated with either method for any given earthquake. Exploiting additional data recorded from 13 temporary stations of which a majority were deployed 2 days after the seismic sequence commenced, we also computed precise relative locations of E2 and its aftershocks using the HypoDD software (Waldhauser & Ellsworth, 2000). GIP3A 1-D seismic velocity model (es&s, 2010; Sandiford, 2013)—a legacy model built into eqFocus program for locating earthquakes in the Gippsland Basin—is used in all our location inversions.

2.2. Focal Mechanisms

We employed the probabilistic approach of Hardebeck and Shearer (2002) to determine focal mechanisms of E1 and E2. This method uses a grid search to determine strike, dip, and slip rake from first motion polarities. The solution space is averaged iteratively. At each iteration, solutions farthest from the average solution are removed until the final cluster of solutions is within a desired range of angles. The misfit of solutions is estimated taking uncertainty in earthquake location, Earth structure model, and polarity picks into account. Computing the intersection point of the ray and the focal sphere accurately for all station-source combinations is important to obtain the best fitting focal mechanism. The intersection point is determined by the take-off angle of a ray, which is a function of earthquake depth and velocity model. In Hardebeck and Shearer's (2002) method, uncertainties in take-off angles, and therefore, uncertainties in focal mechanism solutions, are computed by shooting rays in a range of 1-D velocity models

relevant for the region of interest. The depth from which rays are shot are determined by the earthquake depth and its uncertainty. We used three velocity models for this purpose: VIC5A (Collins, 1988; Wesson, 1988), GIP3A, and ak135-f (Montagner & Kennett, 1996). We provide VIC5A and GIP3A models in Tables S2 and S3 in the supporting information. The solutions are searched for by sampling the focal sphere with a 2° increment.

2.3. Spectral Analysis

We perform spectral analysis of seismograms to compute moment magnitude and stress drop of E1 and E2, where we fit a theoretical spectral function to the average moment rate spectral density function (e.g., Attanayake & Fonseca, 2016).

2.3.1. Moment Rate Spectral Density Functions

Following Houston and Kanamori (1986), we compute moment rate spectral density functions (MRSDFs; equation (1)) from displacement seismograms recorded by short-period stations. In equation (1), $\varphi(f)$ is the P wave MRSDF; ρ and V_p are density and P velocity, respectively, at the hypocenter obtained from GIP3A model; E_R is the radius of the Earth; g is the geometric spreading correction that depends on the source-receiver distance (Δ); R is the radiation pattern correction that depends on the strike (ϕ), dip (λ), and slip rake (δ) of the fault, source-to-station azimuth (γ), and the take-off angle of the ray (ζ); C is the free surface correction that depends on the angle of incidence (ξ); s is the spectrum of the displacement seismogram; t^* is the path averaged attenuation; and f is frequency.

$$\varphi(f) = \frac{4\pi\rho V_p^3 E_R}{g(\Delta)R(\phi,\lambda,\delta,\gamma,\zeta)} s(f)\exp[\pi f t^*] \tag{1}$$

We first automatically mark theoretical traveltimes of the direct P wave based on VIC5A model and then handpick a more accurate arrival time (T_0) using the automatic pick as a guide. The seismogram is then cut within the time window [T_0–0.25 s, T_0 + T_x], where T_0 is handpicked P wave arrival time and T_x is 2.0 s and 1.0 s for E1 and E2, respectively. Based on Stork et al. (2014), T_x was chosen to entirely bracket the direct P waveform and the scattered energy (Figure S1). We compute the spectrum of this windowed seismogram and apply the four corrections given in equation (1) to form the MRSDF of each seismogram. These corrections are described in the next section. The individual MRSDFs are then averaged in $\log_{10}$ space to obtain the average MRSDF of the earthquake, which minimizes the unmodeled residual effects of site, path, and radiation.

2.3.2. Corrections to MRSDFs

2.3.2.1. Geometric Spreading

We use the trilinear geometric spreading model (equation (2)) of Allen et al. (2007) to correct our MRSDFs. This model is developed for southeast Australia using a dense data set covering an epicentral distance up to about 1,000 km.

$$\log_{10} g(\Delta) = \begin{cases} 1.3\ \log_{10}\Delta & \Delta \le 90 \text{ km} \\ 1.3\log_{10}90 - 0.1\ \log_{10}\dfrac{\Delta}{90} & 90\ km \le \Delta \le 160 \text{ km} \\ 1.3\ \log_{10}90 - 0.1\ \log_{10}\dfrac{160}{90} + 1.6\ \log_{10}\dfrac{\Delta}{160} & \Delta > 160 \text{ km} \end{cases} \tag{2}$$

2.3.2.2. Free-Surface Receiver Correction

We correct for the free-surface receiver effect using equation (3) (Bullen & Bolt, 1985). The calculations require the ray emergence angle (e = 90°—incidence angle) at a station, which we computed using the VIC5A model. The range of estimated values is $1.06 \le C \le 1.61$ (~35° < e < ~ 85°), and we find it to be ~1.5 on average. This is consistent with the standard analytical value of 2 used in other studies assuming vertical incidence (Dost et al., 2018).

$$\text{free surface correction} = \frac{6\sin(e)\sec^2(e)[1+3\tan^2(e)]}{4\tan(e)\tan(p) + [1+3\tan^2(e)]^2} \tag{3}$$

where p is defined as follows:

$$\cos^2(p) = \frac{\cos^2(e)}{3}$$

2.3.2.3. Radiation Pattern

The standard practice in studies similar to ours is to use a radiation pattern coefficient averaged over the focal sphere (Abercrombie, 1995). Not accounting for effects of radiation at individual stations accurately, however, can lead to errors of up to 0.8 magnitude units (Stork et al., 2014). For this reason, we opted to correct each MRSDF for radiation pattern following Aki and Richards (2009) using focal mechanism solutions determined in a previous step.

2.3.2.4. Frequency-Dependent Attenuation

Allen et al. (2007) provide a trilinear frequency-dependent attenuation model (equation (4)) for shear waves in Southeast Australia.

$$\log_{10} Q_s(f) = \begin{cases} 3.66 - 1.05\ \log_{10} f & f \leq 3.92 \text{ Hz} \\ 3.01 + 0.03\ \log_{10} f & 3.92\ Hz \leq f \leq 9.83 \text{ Hz} \\ 2.56 + 0.48\ \log_{10} f & f \geq 9.83 \text{ Hz} \end{cases} \quad (4)$$

In equation (3), $Q_s(f)$ is the frequency-dependent quality factor for shear waves and f is frequency. Because there is no P wave attenuation model for our region of study, we scale Allen et al.'s Q_s to P wave attenuation (Q_p) using equation (5) under the standard assumption that bulk dissipation is negligible compared to shear, that is, ${Q_\kappa}^{-1}/{Q_\mu}^{-1} \approx 0$ (Shearer, 1999).

$$Q_p = \left(\frac{3}{4}\right)\left(\frac{V_p}{V_s}\right)^2 Q_s \quad (5)$$

In our scaling, we used $V_p = 6.052$ km/s and $Vs = 3.573$ km/s, consistent with source region velocities given in GIP3A model. This scaled P wave attenuation model is used to correct P wave spectra.

2.3.3. Spectral Fitting and Stress Drop

We fit the spectral function of Boatwright (1978, 1980) given in equation (6) to the average MRSDF of each earthquake and obtain the best fitting moment magnitude and corner frequency. The advantage of using Boatwright's model over Brune's (1970) is that it fits the observed spectral falloff better (Kaneko & Shearer, 2014).

$$\Omega(f) = \frac{M_0}{\left[1 + \left(\frac{f}{f_c}\right)^{2\eta}\right]^{\frac{1}{2}}} \quad (6)$$

Here, $\Omega(f)$ is the source spectrum, M_0 is the seismic scalar moment measured at long periods (scales with moment magnitude M_w), and f_c is the corner frequency, above which the MRSDF falls off at a rate of η. We fit these parameters using a grid search. The search increments are 0.01, 0.1, and 0.1 for M_w, f_c, and η, respectively. The fitting is done for f_x Hz $\leq f \leq$ 50 Hz, where f_x is 0.5 and 1 Hz for E1 and E2, respectively, where the lower cutoff is determined by the length of the time window. Also, the higher-frequency content might be slightly lower for the larger earthquake relative to the smaller earthquake. This, however, does not affect the estimation of magnitude and corner frequency because the frequency band in which these parameters are estimated contains stable source spectra. The best fitting parameters are obtained from minimizing an L_2-*norm* weighted by inverse frequency so that the contribution of each frequency to the misfit is nearly the same. The uncertainties are estimated from fitting parameters to the upper and lower envelopes of the average MRSDF.

We use Eshelby's (1957) radially expanding singular crack model to relate f_c to fault radius (r) and shear velocity at the source (V_s), which can then be used to estimate fault-averaged static stress drop ($\Delta\sigma$; equations (7) and (8)).

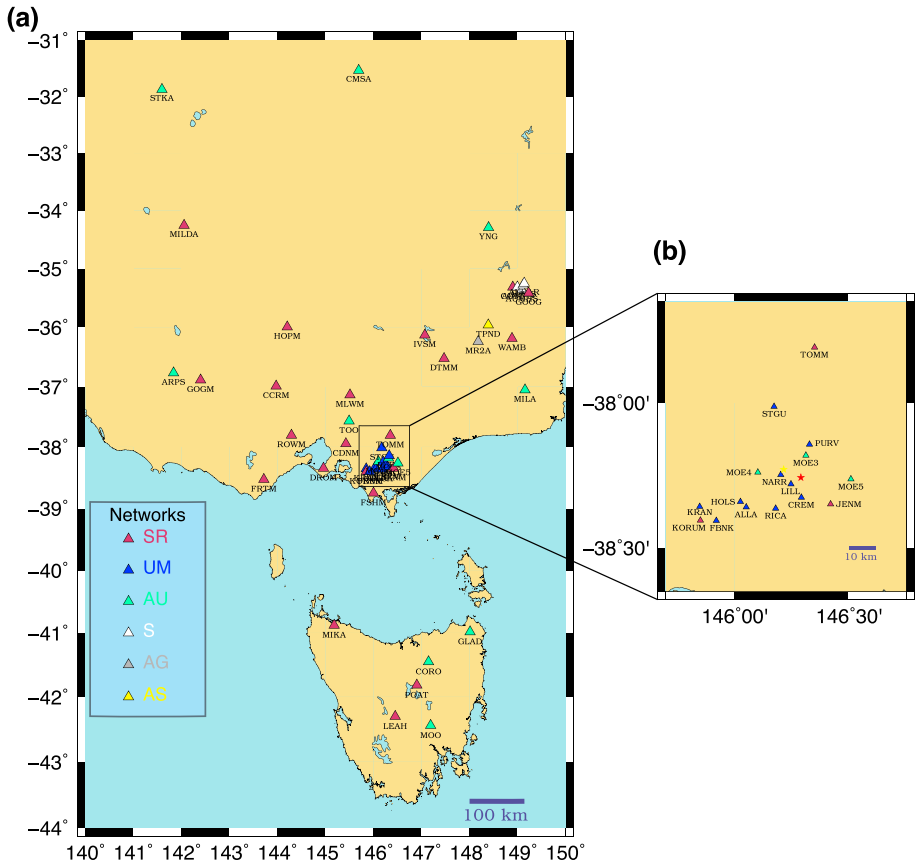

Figure 2. Seismic networks used in this study. (a) Seven networks operated regionally, from which data were acquired. (b) Permanent and temporary seismic stations located within the boxed area in (a). All stations except for SR stations are temporary deployments in (b). The two main shocks relocated in this study are also shown (E1 = red star; E2 = yellow star). AG and AU = Geoscience Australia; AS = Australian Seismological Center; S = Australian Seismometers in Schools; SR = Seismological Research Center network; UM = University of Melbourne.

$$r = k\frac{V_s}{f_c} \tag{7}$$

$$\Delta\sigma = \left(\frac{7}{16}\right)\left(\frac{M_0}{r^3}\right) \tag{8}$$

In equation (6), the proportionality constant k is assumed from a theoretical dynamic rupture model and it depends on the rupture velocity. We used $k = 0.38$ applicable to the cohesive zone circular fault model assuming a rupture velocity of $0.9V_s$ (Kaneko & Shearer, 2014). In section 4 we provide parameters needed to estimate stress drop at different rupture velocities and/or with dynamic rupture models.

3. Data

To analyze the source parameters of the two largest earthquakes in detail, we obtained vertical component waveform data from seven seismic networks for epicentral distances less than 850 km (Figure 2). Forty-three percent (i.e., 23/53) of selected stations from which data were acquired are in the Seismological Research Center network (SR), having a wide flat frequency response spectrum (0.5–50 Hz). We supplemented this data set with data from broadband (0.02–5 Hz) stations in other complementary networks: Geoscience Australia (AU and AG); Incorporated Research Institutions for Seismology (IRIS)/International Deployment of Accelerometers (IDA) (II); privately maintained Australian Seismological Center (AS); and the Australian Seismometers in Schools (S). In addition, we also added stations from temporary networks deployed by the University of Melbourne (UM) and Geoscience Australia to our data set. As mentioned

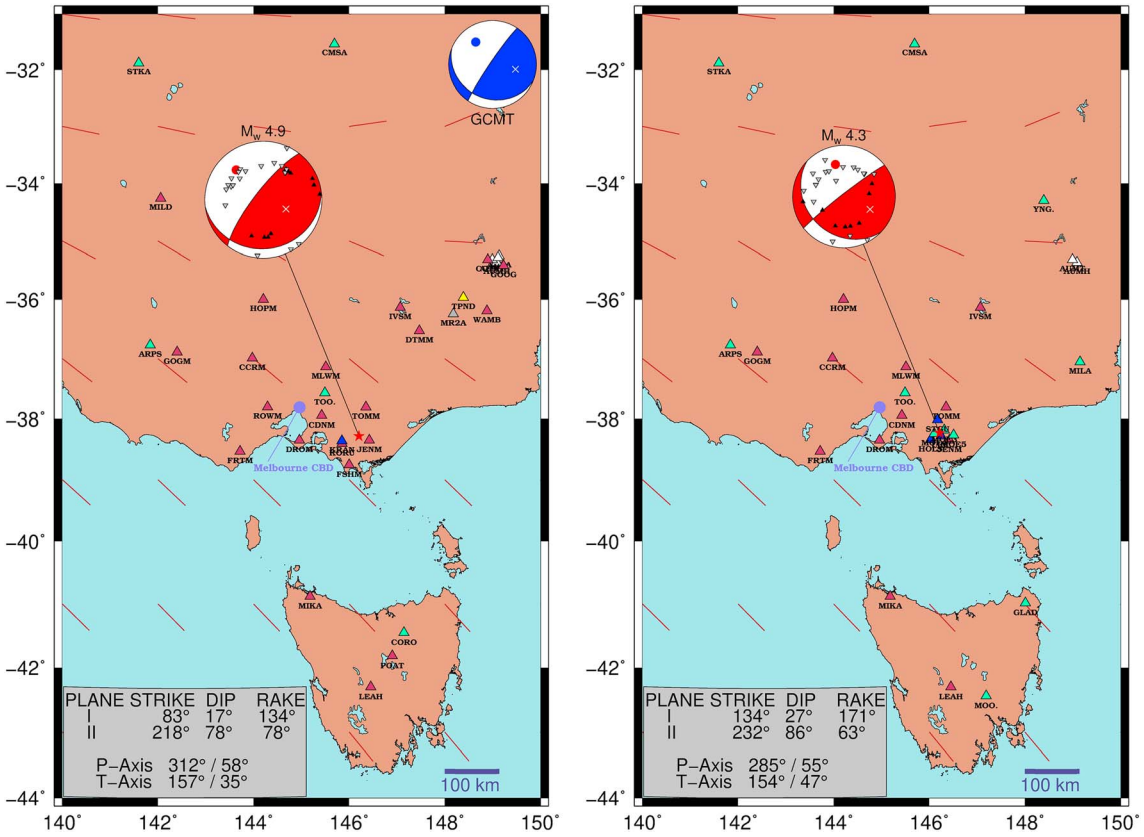

Figure 3. Focal mechanism solutions of 2012.06.19 (left, red star) and 2012.07.20 (right, red star) earthquakes. Also, shown are stations from which data were used. The station color code is the same as in Figure 2. In the focal mechanism, first motion up is illustrated by black triangles, gray inverted triangles show first motion down, and the compressional quadrant is shaded red. Also, shown are *P* (red solid circle) and *T* (white cross) axes. The Global Centroid Moment Tensor solution is also shown for the 2012.06.19 earthquake in the upper right corner of the left panel. The dashed brown lines indicate S_{Hmax} azimuth from Rajabi et al. (2017).

earlier, these included 13 temporary stations progressively deployed in the Thorpdale region 2 days after E1. Given the timeline, this temporary network failed to capture E1 and a majority of its aftershocks, preventing us from performing precise relative locations as was done for E2 and its aftershocks.

We apply standard processing steps to the waveform data, where we remove instrument response and convert counts to displacement. The broadband stations are filtered between 0.02 and 5 Hz, and the short-period instruments are filtered between 0.5 and 50 Hz. Two stations, CCRM and GOGM, had their polarities reversed (Elodie Borleis, Seismological Research Center, personal communication, June 28, 2018), which we correct before finalizing the data set. We retain stations that exhibit excellent signal-to-noise ratio and those whose first motion polarity can clearly be picked. The finalized broadband and short-period data set for these earthquakes (Figure S1) is used to constrain focal mechanisms. Given the wider frequency band of recording and higher sampling period (0.01 s) relative to broadband stations, we use data from short-period stations in our spectral analysis. Hiramatsu et al. (2002) have demonstrated the importance of both these data characteristics for accurate spectral estimates. To locate earthquakes, we precisely pick onset of *P* and *S* waves manually with a picking uncertainty less than 0.03 s. On average, we make 19 combined *P* and *S* traveltime measurements from 11 stations per earthquake.

4. Results

4.1. Focal Mechanisms

Our focal plane solutions and orientations of *PT* axes inverted from first motion polarities (Figure 3) suggest that both E1 and E2 are reverse-faulting earthquakes with some strike-slip component, which is consistent with the compressive stress field predicted for southeastern Australia from numerical modeling (Coblentz

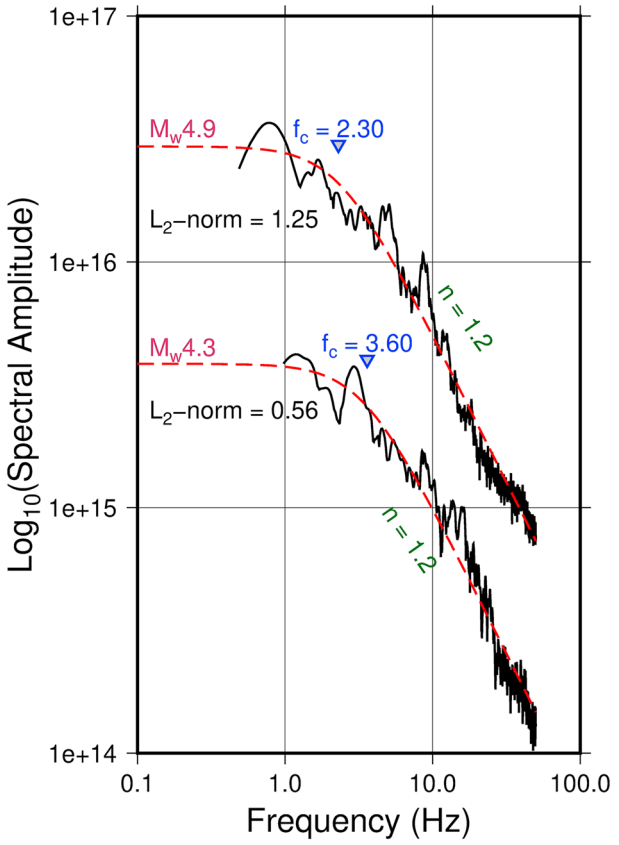

Figure 4. Observed (black lines) and fitted (dashed red lines) source spectra. Parameters obtained from spectral fitting are also given.

et al., 1995) and stress data (Nelson et al., 2006; Rajabi et al., 2017). The solutions for E1 and E2 are obtained from inverting 37 and 28 observations, respectively, with good azimuthal coverage. The Global Centroid Moment Tensor (GCMT) catalog fault plane solutions (Dziewonski et al., 1981) determined for E1, that is, 214°/112° (strike) 85°/22° (dip), and 68°/167° (slip), are consistent with our solutions with reasonable parameter uncertainty and data variability. By decomposing our focal mechanism solutions using Krieger and Heimann's (2012) method, we find that both E1 and E2 resulted from dominant shear faulting (i.e., double-couple component is 99%).

4.2. Earthquake Magnitude, Stress Drop, and Rupture Area

Results of our source spectral analysis are summarized in Figure 4. The scalar moments determined from spectral analysis is (2.6607 ± 1.2000) × 10^{16} and (3.4674 ± 1.0000) × 10^{15} Nm, respectively, for E1 and E2, which translate into M_w 4.9 ± 0.14 and M_w 4.3 ± 0.10. The Global Centroid Moment Tensor magnitude for E1 of M_w 5 is within our uncertainty. Given that we have used new data from stations closer to the source and applied more precise corrections to MRSDFs, we prefer M_w 4.9 to M_w 5. The estimated *fc*, η, *r*, and $\Delta\sigma$ are summarized in Table 2. A η value of 1.2 for both earthquakes is lower than a global average of 1.6 (Allmann & Shearer, 2009) and might indicate premature fault locking, resulting in partial stress drop (Brune, 1986). Alternatively, some combination of rise time and fault area or fault heterogeneity described by a statistical distribution of fault strength could explain this lower falloff rate, for which Hartzell and Heaton (1985) find examples in plate boundary environments. As such, our results suggest that observations of lower spectral falloff rates may also extend to intraplate earthquakes.

Based on recent numerical simulations (Lin & Lapusta, 2018; Zielke et al., 2017), we hypothesize that heterogeneous fault strength at least in part contributed to the difference in stress drop estimates of 57 ± 7.4 (E1) and 28 ± 2.4 MPa (E2). Recall that these estimates are based on Kaneko and Shearer's (2014) Cohesive Zone dynamic rupture model, in which stress drop is a factor of 1.7 smaller than that estimated from Madariaga's (1976) dynamic rupture model. This difference results from different *k* values: Kaneko and Shearer's $k = 0.38$ versus Madariaga's $k = 0.32$ for a rupture velocity of $0.9V_s$. We prefer Kaneko and Shearer's *k* value because they take 3-D wave propagation effects into account better than, for example, Madariaga's (1976). Also, Kaneko and Shearer's dynamic model incorporates a cohesive zone that prevents a stress singularity in the rupture front. These models describe cohesive forces active in a crack better. If the assumption of a rupture velocity of $0.9V_s$ is relaxed to a lower value, the estimated stress drop increases. We note that our estimates of stress drop with a rupture velocity of $0.9V_s$ are comparable with predicted lithospheric averaged, differential stress magnitudes of ~20–50 MPa in southeastern Australia (Coblentz et al., 1995). We provide necessary parameters in Table 2 for computation of stress drop for other rupture models and velocities.

Taken together, *fc*, reduced η, and $\Delta\sigma$ indicate the possible rupture of strong, relatively small asperities as observed in earlier investigations (Kanamori & Allen, 1986). In fact, our analysis suggests that the estimated source area (1.1 km^2) of E1 is only ~25% of that expected for an average rupture of similar magnitude (4.4 km^2) from scaling relationships applicable to intraplate regions (Leonard, 2010). However, the distribution of aftershocks following E1 and E2 in the first 24 hr suggests that the fault area expanded following the main shocks. We discuss this further in the next section.

Dawson et al. (2008) estimated source parameters of a rare M_w 4.7 earthquake located in the southwestern seismic zone in Western Australia

Table 2
Estimated Source Parameters of E1 Located at a Depth of 18.1 km (Line 1) and E2 (Line 2) Located at a Depth of 12.4 km

Event date	M_w	f_c	*r* (km)	η	$\Delta\sigma$ (MPa)
2012.06.19	4.9 ± 0.2	2.3 ± 0.1	0.59	1.2	57 ± 7.4
2012.07.20	4.3 ± 0.1	3.6 ± 0.1	0.40	1.2	28 ± 2.4

Note. M_w = moment magnitude; f_c = corner frequency of average source spectrum; *r* = radius of the equivalent circular rupture; $\Delta\sigma$ = stress drop.

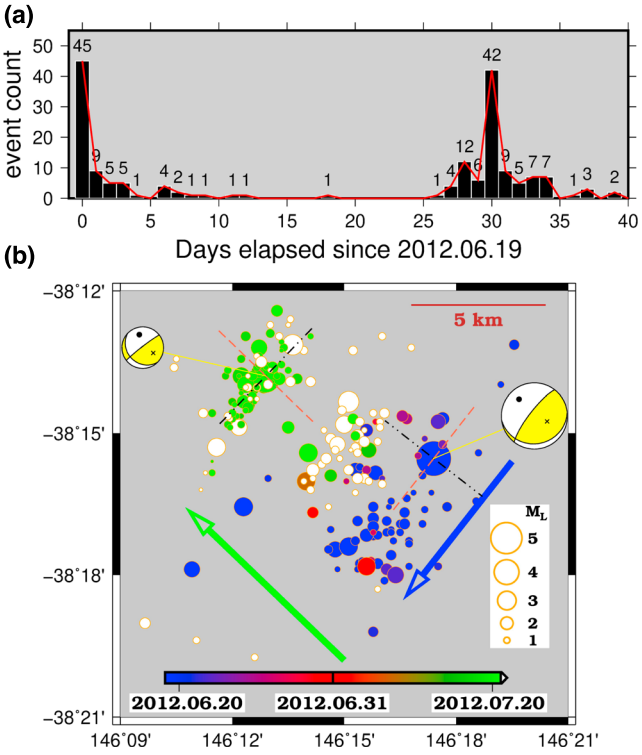

Figure 5. Spatiotemporal evolution of earthquakes. (a) Temporal distribution of frequency of earthquakes in the first 40 days following E1. Two peaks associated with E1 and E2 are clearly observed. Numbers on top of each column indicate the number of earthquakes on that particular day. The red line connects the columns to illustrate earthquake rate. (b) The epicenters color coded by elapsed time. The color scale is for the time period 19 June 2012 to 20 July 2012, and earthquakes falling outside this time range are colored white. Focal mechanism solutions are also mapped on to epicenters of E1 and E2. The arrows indicate the general direction of seismicity migration immediately following E1 (blue) and before E2 (green). Pink dashed lines are the strike directions of preferred fault planes of E1 and E2, whereas the dash-dotted black lines are orthogonal to the preferred strike directions. These directions are used in the projections given in Figures 6 and 7.

using interferometric synthetic aperture radar modeling. They estimated stress drop and fault rupture area to be 53 MPa for a distributed slip model and ~1 km^2, respectively, which is remarkably consistent with the M_w 4.9 earthquake investigated in this study despite using different methods. We find that the rupture area estimated by Dawson et al. (2008) is also only 16% of that expected from global scaling relationships for an earthquake of similar magnitude. Note that the magnitude of the compressive stress field in Western Australia is similar to that in southeastern Australia (Coblentz et al., 1995; Denham et al., 1987). These observations raise the question whether moderate-sized seismic sources modulated by a high compressive stress magnitude in the Australian continent are self-similar. Testing this hypothesis requires more data.

4.3. Earthquake Location

In total, we located 236 earthquakes between 1 January 2012 and 11 April 2018 with $M_L \geq 0$. Prior to 19 June 2012, only two small earthquakes (M_L = 1.2 and 1.8) had occurred in January and April of 2012 in Thorpdale. This suggests that the seismic sequence in Thorpdale commenced with E1. In Figure 5, we show earthquake rate and a map of epicenters whose source parameters are given in Table S1 in the supporting information. The distance to the nearest station from E1 (JENM, ~15 km) and E2 (NARR, ~2 km) is less than their respective hypocentral depths (E1 = 18.06 km and E2 = 12.41 km), providing high confidence in the source locations. The addition of temporary stations reduced the distance to the nearest station from any given aftershock to less than 5 km from about 15 km prior to installing the temporary stations, which is generally less than source depths estimated in this study. Numerical experiments demonstrate that when both P and S waves are used in source location inversion, accurate source depths can be obtained when the distance to the nearest station is ~1.4 times the source depth (Gomberg et al., 1990). Given that the distance to the nearest station in the first 2 days of the seismic sequence was ~15 km, this suggests that source depth of aftershocks located at depths greater than ~11 km are well constrained. In our catalog, about 69% of aftershocks in the first 2 days were located at depths greater than 11 km. These favorable geometric conditions reflect the average uncertainty of ± ~2 km in our source locations.

The hypocentral separation between E1 and E2 increases to ~9.2 km from the U.S. Geological Survey preliminary estimate of ~5 km, which is well beyond the fault dimensions determined from our spectral analysis. This hypocentral separation is also significantly larger than the average area (proportional to length of a fault) expected for a single earthquake in an intraplate setting of similar size (Leonard, 2010) even after accounting for lateral and vertical location uncertainty of ~2 km. This naturally raises the question whether E2 ruptured the same fault plane as E1. Analysis of spatiotemporal characteristics of the seismic sequence provides evidence to resolve this problem.

4.3.1. Spatiotemporal Evolution of the Seismic Sequence

Two clear peaks are visible in Figure 5a where we show earthquake rate following E1. We were able to record smaller earthquakes ($M_L < 1$) as a result of deploying temporary stations several days after E1 occurred. In fact, all earthquakes (29 in total) with $0 \leq M_L < 1$ are associated with E2 in this study. The peak associated with E1 is one sided, meaning no precursory activity was recorded with at least M_L 1. There is a rapid decrease in aftershock activity after the first 24 hr, which is also observed in other large intraplate earthquakes (e.g., Copley et al., 2012). On the other hand, a two-sided peak is associated with E2. We observe that seismic activity picked up 4 days before E2 and dropped markedly in as many days after E2 with a majority of these earthquakes having a magnitude $M_L > 1$. This suggests that the seismic sequence commenced with E1, and some precursory activity preceded E2.

In Figure 5b, the evolution of the seismic sequence is illustrated for the time period 19 June 2012 to 20 July 2012. We observe that a majority of the aftershocks in the first 24 hr following E1 (blue solid circles) are clustered in a southwest direction from E1, implying that fault plane expanded in that direction. Within the aftershocks cluster, however, we do not observe a systematic migration of seismicity. We elaborate this later in section 5.2. The general alignment of these aftershocks relative to E1 is consistent with the strike of the steeper focal plane of E1, that is, 218° (strike), 78° (dip), and 78° (slip rake). Although the aftershock activity diminished considerably after 24 hr, it appears that the migration of seismicity changed from an initial SW direction to a NW direction in the days following E1 (dark-to-bright red to brown circles) and culminated in E2 and associated aftershocks. Unlike aftershocks of E1, a significant number of aftershocks of E2 are collocated. These observations suggest the activation of a fault plane striking SE-NW.

The depth of aftershocks associated with E1 and E2 are also characteristically different (Figure S2 in the supporting information). The aftershocks of E1 are distributed in the 10- to 18-km-depth range, whereas those that are associated with E2 are contained within 5- to 15-km depth. In fact, E1 appears to be located at the bottom of the seismogenic layer, which we estimate to be 18–20 km thick based on our results. Leonard's (2008) estimates of the thickness of the seismogenic layer in Australia based on a 100-year seismic catalog is similar to what we predict here.

4.3.2. Did E1 and E2 Rupture Different Faults?

To resolve the orientation of the faults that were activated, we project seismicity on to cross sections parallel and perpendicular to strike directions given by focal mechanism solutions (Figures 6 and 7). We divided the earthquake data set into two subsets: (a) from 19 June 2012 to 30 June 2012 that captures seismicity associated with E1 (Figure 6) and (b) from 15 July 2012 to 30 July 2012 that captures the sequence associated with E2 (Figure 7). Figure 6c is the cross section perpendicular to the fault plane solution 218°/78 °/78° of E1 on to which E1 and its aftershocks are projected, and we find that earthquakes are clearly aligned with the steeper plane (218°/78°/78°) as opposed to the shallow-dipping one (83°/17°/134°). Thus, we conclude that E1 activated the steeper plane. Similarly, in Figure 7c, we project E2 along with its aftershocks perpendicular to the fault plane solution 134°/27°/171°. There, the earthquakes are aligned with the shallow-dipping plane (134°/27°/171°) rather than the steeper plane (232°/86°/63°) of E2. Therefore, we suggest that E2 activated the 134°/27°/171° plane. Based on these projections, it seems that E1 activated a different plane than E2. Henceforth, we use Fault 1 (E1) and Fault 2 (E2) to describe 218°/78 °/78° and 134°/27°/171° planes, respectively.

5. Discussion

5.1. Links to History of Deformation

Within the framework of Coulomb failure criteria, bimodal conjugate systems of faults are predicted with a maximum interplane angle of 60° (Anderson, 1905). The interplane angle for Fault 1 and Fault 2, however, is nearly orthogonal, suggesting that these faults originated from different deformation episodes. Fault 1 is optimally oriented relative to the inferred present-day maximum horizontal stress (S_{Hmax}; Figure 3) to be reactivated with reverse motion as demonstrated in slip tendency analysis (Müller et al., 2012). In southeast Australia, the origin of faults having a similar orientation to Fault 1 are traced back at least to the early Pliocene (Sandiford, 2003). Thus, if Fault 1 and Fault 2 do not belong to the same conjugate system, it might be that Fault 2 dates to an early stage in Fault 1. This is consistent with the inference from modeling presented by Sandiford et al. (2004), for a progressive Paleogene-Neogene counterclockwise rotation in S_{Hmax}.

Etheridge et al. (1987, 1991) reported the observation of a shallow-dipping normal fault system with a 295–300° strike in the offshore Gippsland Basin. This fault system formed as Australia rifted from Antarctica in the early-to-late Cretaceous, and it was reactivated with a reverse sense (inversion) in the middle Eocene. A conjugate set of this particular fault system could then explain the orientation of Fault 2. Considering mechanics of faulting, the present-day fault configuration requires a history of regional-scale polyphase deformation including block and stress rotation (Dembo et al., 2015; Ron & Beroza, 2001; Sibson & Xie, 1998; Zoback, 1992). Evidence supporting these processes is present in the geologic record of southeast and east Australia (Dickinson et al., 2002; Fielding et al., 2016; Quigley et al., 2010; Sandiford & Quigley, 2009; Vandenberg, 2010). Numerical experiments also suggest that the stress field in southeast Australia has undergone significant rotation since circa 55 Ma (Müller et al., 2012; Sandiford et al., 2004).

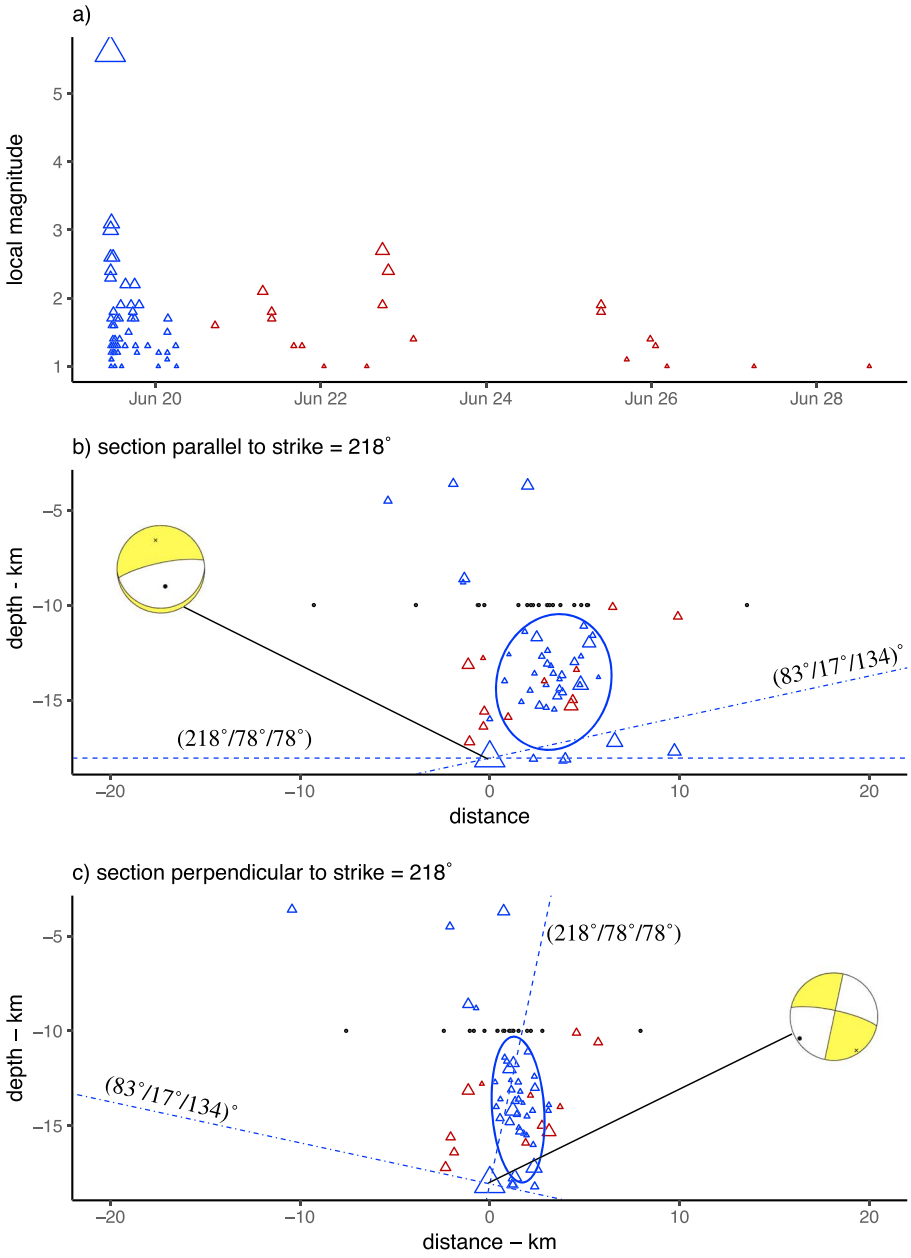

Figure 6. The projection of earthquake hypocenters on to cross sections. (a) Earthquake distribution from the 19 June 2012 to 30 June 2012 period. The blue and red open triangles are E1 and its aftershocks color coded by time, where the size of triangles scale with their local magnitudes. (b) The projection of fault plane solutions and earthquakes in (a) on to a cross section parallel to the strike 218°. The horizontal distance is relative to the location of E1. The ellipse arbitrarily envelopes the region where the aftershock density is highest. The focal mechanism of E1 is also projected to this cross section. (c) Same as (b) but the projection is on a cross section perpendicular to the strike 218°. The earthquakes are clearly aligned with the 218°/78°/78° plane. Also, see Figure 5 for the map view of projection orientations.

Alternatively, the origin of these faults might be a polymodal process, in which case they are coeval structures responding to the 3-D stress field (Healy et al., 2015; Oertel, 1965). To the South of the Thorpdale seismic sequence, numerous faults with a general NE-SW strike and an irregular interval cut through the Strzelecki group and intrusive granites of lower Cretaceous and upper Devonian origin, respectively (Figure S3 and S4 in the supporting information). Embedded in this fault network is a sparsely distributed secondary fault network with a WNW-ESE strike (e.g., Franklin fault, Vagg Creek fault, and Balook fault). Fault 2 aligns with this secondary network of faults well. If a more recent date than middle Eocene (e.g.,

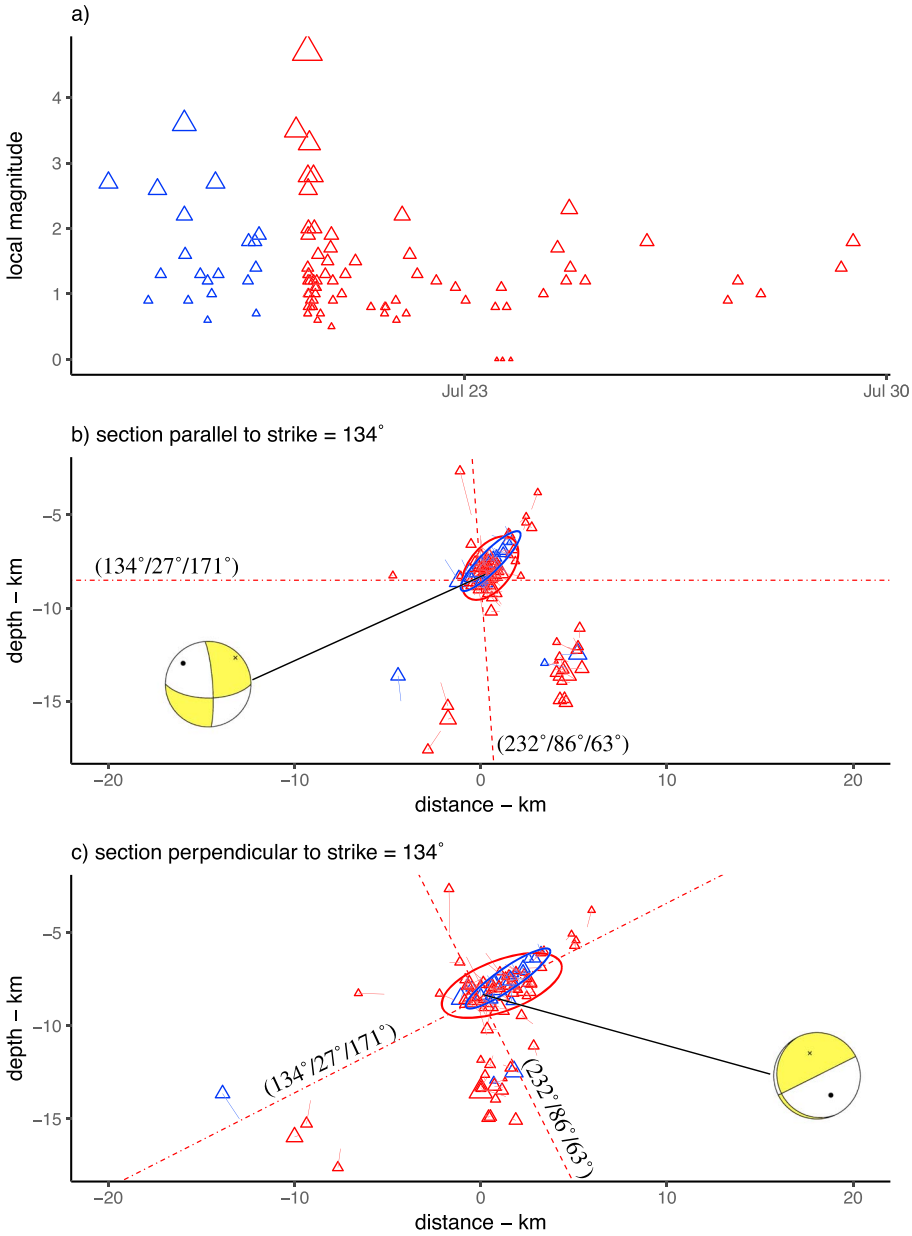

Figure 7. This is the same as Figure 6, but seismicity is for the time period from 15 July 2012 to 30 July 2012, capturing E2 and its aftershocks located with double-differencing method. Also, the cross sections are (b) parallel and (c) perpendicular to a strike of 134°. Stronger clustering of earthquakes is observed, and a majority of earthquakes align with the shallow-dipping plane as seen in (c). Also, see Figure 5 for the map view of projection orientations.

Etheridge et al., 1987) can be established for these faults, a polymodal mechanism cannot be ruled out given that observations of polymodal faults have been made in NE Australia (Carvell et al., 2014).

5.2. Stress Buildup and Release

Coulomb stress transfer modeling offers a useful way to evaluate if E1 triggered E2 (Lin & Stein, 2004; Stein, 1999; Stein et al., 1997; Toda et al., 2005; Walsh et al., 2015). We used the U.S. Geological Survey software Coulomb (available at http://earthquake.usgs.gov/research/modeling/coulomb/; Lin & Stein, 2004; Toda et al., 2005) to quantify changes in the regional Coulomb failure stress ($\Delta\sigma_{CF}$) imparted by E1 to determine if E2 was triggered due to static stress transfer. The expectation for such a relationship is an increase in $\Delta\sigma_{CF}$

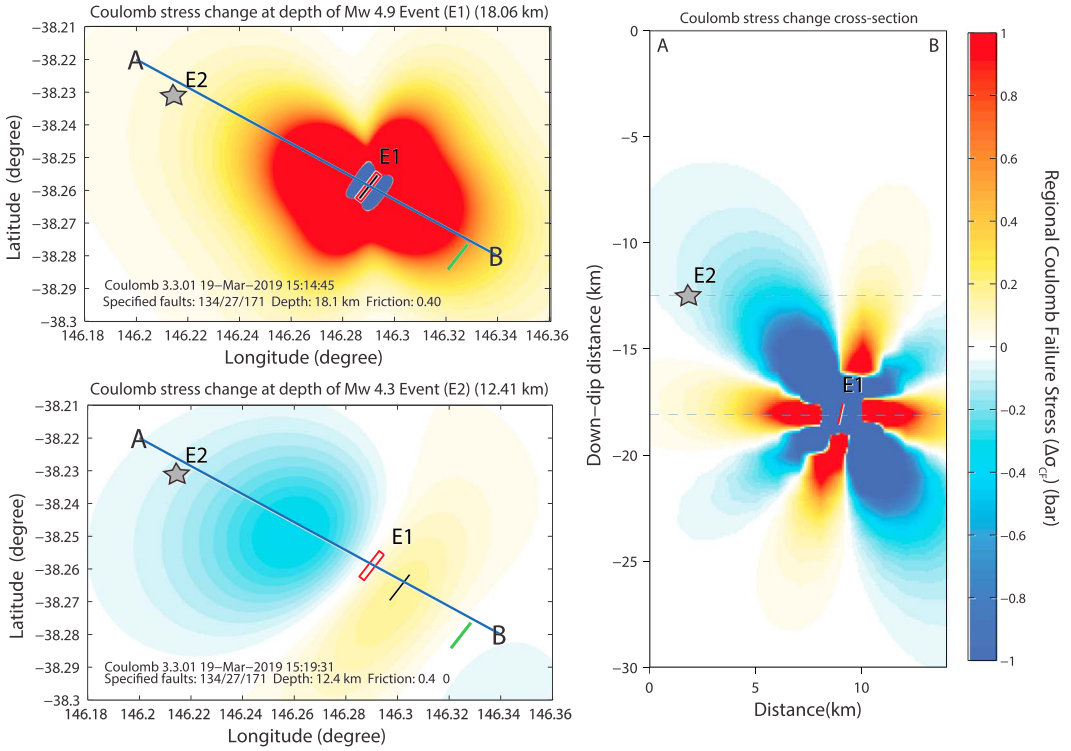

Figure 8. Regional Coulomb failure stress change ($\Delta\sigma_{CF}$) imparted by E1 to receiver faults parallel to the rupture plane of E2. The focal mechanism primary rupture plane with an orientation of 218° (strike), 78° (dip), and 78° (slip rake) was used for the source fault orientation. The $\Delta\sigma_{CF}$ field was resolved on receiver fault planes parallel to E1 with an orientation of 134° (strike), 27° (dip), and 171° (slip rake). The red box shows the rupture plane of E1 (1.1 km × 1 km) at its hypocenter, and E2 is shown by the gray star. The upper left panel shows $\Delta\sigma_{CF}$ at the hypocentral depth of E1 (18.1 km), whereas the lower left panel shows that at the hypocentral depth of E2 (12.41 km). The right panel illustrates $\Delta\sigma_{CF}$ on a cross section between A and B.

on E2 as a result of E1. The magnitudes of $\Delta\sigma_{CF}$ need not be large and typically is greater than +0.01 MPa where the relationship is held to be causal (King & Cocco, 2001).

In this analysis, we used a coefficient of apparent friction of $\mu' = 0.4$, a shear modulus of 32 GPa, and a Poisson's ratio of 0.25, which are similar to other stress transfer calculations covering a variety of rock types (King et al., 1994; Toda et al., 2005). We also set the along-strike fault length to 1.1 km and down-dip width to 1 km so that the fault area estimated from spectral analysis (~1.1 km^2) remains fixed. We used the primary plane from the focal mechanism solution (218°/78°/78°) of E1 and predict the σ_{CF} imparted to the primary focal mechanism plane (134°/27°/171°) of E2 (Figure 8).

Figure 8 shows that $\Delta\sigma_{CF}$ on E2 decreased slightly by ~0.008 MPa and, on face value, negates expectation for stress coupling as the causal mechanism for E2. Therefore, we infer that accumulation of stresses over time from tectonic forces and prior events may have generated a baseline stress field conducive for nucleating E1 and E2 in a rapid succession and that the slight reduction in $\Delta\sigma_{CF}$ would have been too small to change those initial conditions. Notwithstanding an apparent lack of static stress coupling, it is intriguing that E1 and E2 are clustered in time and space. In the next subsections, we explore some other possible scenarios.

Seismic sequences exhibiting coupled fault behavior are found elsewhere in Australia. For instance, the four largest earthquakes (M_s 6.3, 6.4, 6.7, and 5.3) in Tennant Creek occurred within a 20-hr period on 22 January 1988 with a hypocenter separation of less than 15 km (Bowman, 1992; Jones et al., 1991). Focal mechanism solutions indicate that the interstrike angles of these earthquakes were 118–133°, suggesting the activation of a complex fault system. In addition, McCue (1990) documents other large earthquakes ($6 \leq M_L \leq 6.6$) that are clustered in time and space. Thus, it appears that Australia is a candidate intraplate region for producing

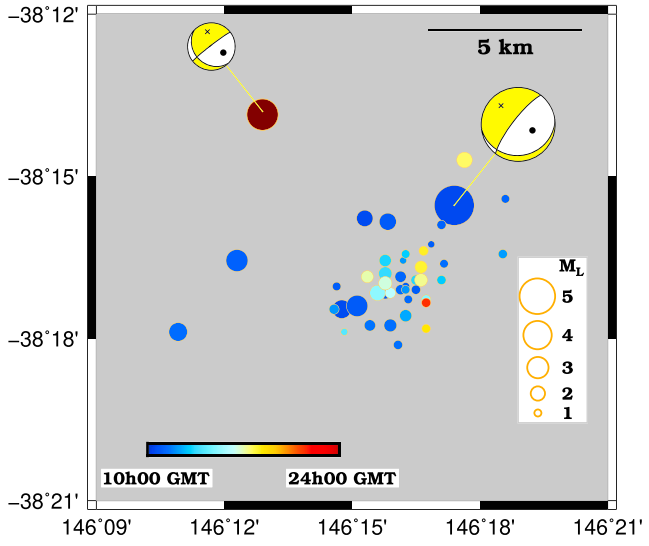

Figure 9. Spatiotemporal evolution of seismicity on 19 June 2012 between 1000 and 2400 hr. Aftershocks of E1 are clustered to the southwest of E1. Within the aftershock cluster, however, seismicity do not show a discernible spatial pattern. These aftershocks occur in a region where $\Delta\sigma_{CF}$ = ~ +0.1 MPa (see Figure 8). The M_w 4.3 earthquake is shown in maroon color.

clustered complex fault ruptures. To what extent a high compressive stress magnitude (Coblentz et al., 1995, 1998; Nelson et al., 2006) in the crust contributes to this behavior of faults needs further investigation. Future work to map the changes in stress over time in the region including the effect of prior seismicity may provide additional information regarding the state of stress and mechanism for triggering E2.

5.3. Rotation of the Local Stress Field

A stress drop of E1 on the order of differential stress (i.e., $\sigma_1 - \sigma_3$) in the crust can produce a localized, transient rotation of the stress field (Hardebeck & Okada, 2018 and references therein), which can preferentially orient the local stress field temporarily to promote rupture on faults suboptimally oriented. Using Yin and Rogers' (1995) equations and principal stress magnitudes estimated by Nelson et al. (2006) for the Gippsland Basin, we estimated that E1 rotated the local stress field by about 10° toward the normal to Fault 1. *P* axis orientation determined from focal mechanism solutions also suggests that the direction of principal compression rotated by 27° counterclockwise, consistent with inferred left lateral motion of E1. Whether this stress field rotation reoriented Fault 2 favorably for failure needs further investigation given that there is a nonlinear relationship between Coulomb stress and the orientation of principal stress axes (King et al., 1994). While such rotations are not captured in our Coulomb tests, they have been previously recognized as important for triggering earthquakes on low-angle fault planes in numerical experiments (Wills & Buck, 1997).

5.4. Fluid Diffusion-Assisted Seismicity

An alternative hypothesis for causal linking of sequential rupture on nearby but distinct faults is fluid diffusion-assisted seismicity migration (Chen et al., 2012; Talwani et al., 2007). Previous observations and modeling suggest that this process is likely to span a short time window (hours to days) within which the earthquakes are clustered (Hummel & Müller, 2009; Yukutake et al., 2011). Also, fluid-induced seismicity is characterized by smaller stress drop values because introducing fluids lubricates faults, reducing effective shear resistance (Hough, 2014; Yamada et al., 2015). Analyzing tectonic and induced earthquakes in the central Unites States, Huang et al. (2017), however, claim that fluid-induced and natural earthquakes are indistinguishable in terms of stress drop. Nonetheless, when taken together, time window of occurrence, temporal evolution, and stress drop should allow for identifying fluid-assisted seismicity migration.

Our catalog indicates that 44 aftershocks occurred following E1 on the same day and that seismicity was active at least up until April 2018 with a diminishing rate, suggesting a period of prolonged stress release. Aftershocks within the first 24 hr do not show a discernible spatial pattern (Figure 9) as would be expected for rapid fluid diffusion-driven seismicity (Yoshida & Hasegawa, 2018). Instead, we observe that these aftershocks were triggered in a random pattern, consistent with the rupture of smaller asperities on the fault as those locations were loaded to failure from static stress transfer (Goebel et al., 2012; Kazemian et al., 2015). This is consistent with our predictions of $\Delta\sigma_{CF}$, where these aftershocks are located within a region to the southwest of E1 with $\Delta\sigma_{CF}$ up to +0.1 MPa. Thus, it is unlikely that a fluid-assisted process activated E1 and its immediate aftershocks.

With an apparent lack of stress coupling between E1 and E2, however, we cannot rule out fluid diffusion activating E2. The stress drop of E2 being nearly one half that of E1 might suggest lubrication of Fault 2, by which shear resistance at the fault interface is reduced. Another feature that supports this hypothesis is precursory activity that began 2 days prior to the occurrence of E2 nearly at the same location as E2 (Figures 5 and S2). Delayed sluggish release of previously locked pore fluid in the vicinity of E2 from shaking effects of E1 might have triggered these smaller precursory earthquakes, which in turn enhanced permeability in the rock rather rapidly. A resulting diffusion of fluid could have reduced clamping stress on an extended fault interface, producing a larger event (E2). Global data sets provide evidence for such a

remote and delayed triggering mechanism (King & Cocco, 2001; Parsons et al., 2017). Detailed knowledge of fluid diffusion in this region is required to test this hypothesis, which would be important future research work.

5.5. Implications to Seismic Hazard

It is difficult to ascertain if E1 is a characteristic earthquake for this region without paleoseismic evidence. Nonetheless, it is important to constrain parameters useful for seismic hazard analysis of similar earthquakes. Stress drop estimate is a key input parameter in strong ground motion simulations as they determine the high frequency acceleration (Baltay et al., 2013). Also, the variability of stress drop between the two earthquakes studied here contributes to the variability of strong ground motion models, which is an important consideration in seismic hazard analysis (Cotton et al., 2013; Oth et al., 2017). It would be interesting to test if the peak ground acceleration of 0.8 m/s^2 calculated for southeastern Australia (Gaull et al., 1990) should be revised based on our estimates of stress drop.

Taking a physics-based approach, recurrence interval is another important parameter that we can constrain. The strain drop ($\Delta\varepsilon$) associated with earthquakes can be estimated from $\Delta\sigma/\mu$ (Kanamori & Brodsky, 2004), where μ is the dynamic shear modulus estimated from (shear velocity)^2 × density. We obtained these values for the hypocenter from the GIP3A model and find that E1 and E2 have $\Delta\varepsilon$ of 1.809×10^{-3} and 8.61×10^{-4}, respectively. The recurrence interval can then be calculated as $\Delta\varepsilon/\hat{e}$, where $\hat{e}$ is the average strain rate for the region (Ward, 1998). If we use Sandiford et al.'s (2004) upper bound of 3.153×10^{-9} $year^{-1}$ for $\hat{e}$, we obtain 573 and 273 ka, respectively, for E1 and E2. Regardless of appreciable uncertainty, these physics-based estimates agree to a first order with those obtained from field investigations in the region (Gardner et al., 2009).

The high stress drop-long recurrence relationship is explained by the phenomenon called "stiction," where static friction increases with stationary contact time of fault interfaces (Dieterich, 1972; Gitis & Volpe, 1992). The increase in static friction coupled with other processes such as chemical healing increases shear resistance (fault strength), requiring larger stresses to initiate rupture. The observation of higher stress drop in intraplate environments than in interplate ones (Allmann & Shearer, 2009; Romanowicz & Ruff, 2002; Scholz et al., 1986) can thus be explained by the time dependence of shear resistance.

5.6. Global Implications

Although intraplate seismicity accounts for less than 5% of global moment release (Talwani, 2014), both historical and contemporary examples indicate a disproportionate damage to life and property from it (Bilham, 2014; Bodin & Horton, 2004; Ming et al., 1995). Despite this, forecasting hazard from intraplate earthquakes is difficult primarily because faults remain undetected prior to rupturing, it is difficult to detect active segments of mapped faults due to long quiescence periods, or earthquake characteristics are not well constrained due to the short temporal record of seismicity (Wolin et al., 2012). Thus, comparing information across analogous intraplate environments is useful for understanding geologic conditions under which these earthquakes occur, and their characteristics.

5.6.1. Influence of Heat Flow

Global observations of intraplate seismicity (e.g., central and eastern North America, China, western India, Australia, and Africa) are generally attributed to either reactivation of preexisting zones of mechanical weakness such as rifted crust (Schulte & Mooney, 2005; Stein et al., 2014; Talwani & Rajendran, 1991), local geologic structures and dynamics favorable for stress concentration (Attanayake & Fonseca, 2016; Dentith & Featherstone, 2003; Forte et al., 2007; Levandowski et al., 2018; Stephansson et al., 1991; Talwani, 2014), or thermomechanical weakening of the lower crust and the upper mantle (Célérier et al., 2005; Kenner & Segall, 2000; Liu & Zoback, 1997).

Based on previous studies, seismicity in Gippsland Basin, (Thorpdale is located within the Gippsland Basin) can be linked to at least two of the above mechanisms, namely, reactivation of faults generated by rifting of Australia from Antarctica in the Lower Cretaceous (Etheridge et al., 1987, 1991) and thermomechanical weakening of the lower crust and the upper mantle (Holford et al., 2011; Sandiford & Egholm, 2008). Clark et al. (2014), however, argue against the control of thermomechanical weakening on the basis of relatively low levels of seismicity and neotectonics features in the Cooper/Eromanga Basin in east central Australia, where some of the largest heat flow anomalies in Australia are observed.

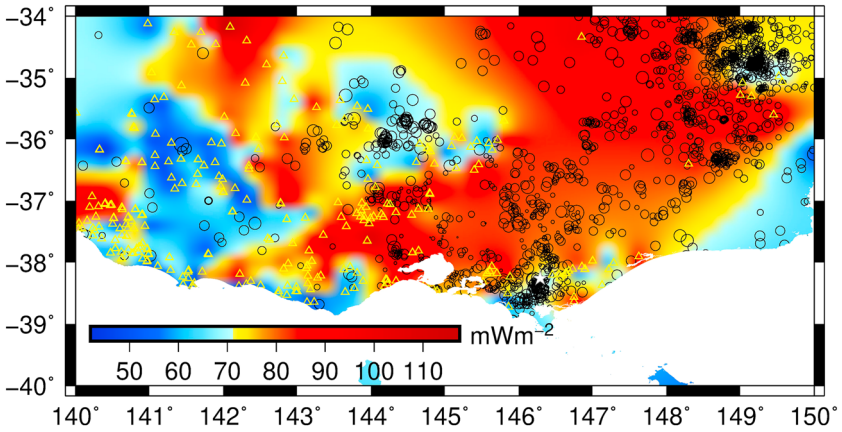

Figure 10. Interpolated heat flow field and seismicity from Figure 1. The locations of heat flow measurements and earthquakes are shown with triangles and circles, respectively. The radii of circles scale with earthquake magnitude. The location of Thorpdale seismic sequences is shown by the white star. An apparent correlation between high heat flow and seismicity emerges in this map.

To test this hypothesis, we combined new heat flow measurements of Mather et al. (2018) with those of Holford et al. (2011) to produce a map of heat flow field of southeast Australia using a minimum curvature interpolation approach (Smith & Wessel, 1990) and overlay 51 years of seismicity (Figure 10). Notwithstanding limitations in heat flow data coverage, an apparent correlation between heat flow field and seismicity emerges, where regions that are seismically most active have an apparent heat flow > ~70 mW/m^2. A similar apparent correlation has been observed by Holford et al. (2011) primarily in the Flinders Range Seismic Zone in south Australia. Anomalous low seismic velocities are observed in the upper mantle beneath this region of high surface heat flow (Davies et al., 2015; Rawlinson et al., 2016), consistent with somewhat elevated Moho temperature and a mechanism involving weakening of the lower crust and upper mantle as Liu and Zoback (1997) proposed for the New Madrid Seismic Zone (NMSZ).

Liu and Stein (2016) argue that weakening from rifting is neither necessary nor sufficient for intraplate deformation based on observed seismicity in the NMSZ and north China. Recent quantitative analysis suggests, however, that structural inheritance from past tectonic cycles observed in the Saint Lawrence Valley in eastern Canada is an important factor in driving present-day intraplate deformation, where the strain rate can be 2 to 11 times higher than the surrounding region (Tarayoun et al., 2018). This latter study assumes that no other process contributes to observed high deformation rates. On the other hand, our analysis suggests that, even if high heat flow is not solely responsible for localizing deformation, it is likely a contributing factor.

5.6.2. Fault Behavior

A common feature observed in several major intraplate environments including Australia, North China, and the NMSZ is the spatiotemporal clustering of earthquakes followed by prolonged quiescent periods ranging from hundred- to million-year timescales (Calais & Stein, 2009; Clark et al., 2012, 2014; Crone et al., 2003; Liu & Stein, 2011). In southeast Australia, sparse data suggest quiescent periods of the order of ~100 ka (Gardner et al., 2009), consistent with our prediction in this study.

Liu et al. (2011) explain the behavior of intraplate faults using the concept of complex dynamic systems, in which slow tectonic loading is accommodated in a distributed network of interacting faults, and nontectonic variable transient stress perturbations (e.g., static stress transfer, isostatic adjustment to erosion, and local stress field rotation) controlling the triggering of earthquakes. For instance, we hypothesize that interplay between transient stress conditions and fluid diffusion may have coupled E1 to E2 in this study. On the other hand, static stress transfer has been identified to increase seismic potential in other intraplate environments. For example, Walsh et al. (2015) estimated that neighboring faults within about 10 km were loaded by as much as 0.05–0.5 MPa following the M_w 5.8 earthquake in Mineral, Virginia, in 2011. This level of static stress change is capable of producing secondary main shocks (Stein, 1999).

Within Liu et al.'s (2011) framework, the opposite effect is also feasible. That is, if an earthquake produces a stress shadow, earthquakes on receiving faults will be suppressed or delayed. For example, Liu et al. (2018)

suggest that the magnitude of the 2008 M_w 7.9 Wenchuan intraplate earthquake in China was suppressed by a long-term stress shadow produced by 283 years of seismicity in and around the Longmen Shan Fault preceding the Wenchuan earthquake. Also, Li et al. (2005) predict a similar stress shadow scenario for the present-day NMSZ, where three M_w 7.0–7.5 earthquakes occurred in 1811–1812. In our case, however, we find that the negative static stress coupling is too weak to hinder the failure of Fault 2. Therefore, if Liu et al.'s (2011) model accurately describes intraplate fault behavior, it becomes a challenge to understand the utility of commonly used concepts such as recurrence interval, $M_{\max}$, and fault slip rate in seismic hazard analysis because these estimates become highly dependent on transient stress perturbations (Calais et al., 2016). As Stein and Liu (2009) pointed out, it may be that hazard in regions where faults have been recently active is overestimated, whereas that in other regions that lack recent seismicity is underestimated. Innovative seismic hazard analysis methods are needed to capture the effects of intraplate seismicity driven by transient processes.

6. Conclusions

We located 234 earthquakes of the 2012 Thorpdale seismic sequence and estimated source parameters of the two largest earthquakes (E1 and E2) to understand the rupture process. Our focal mechanism solutions suggest reactivation of faults in a reverse sense, consistent with the regional compressive stress field. From our source spectral analysis, we estimate earthquake magnitudes to be M_w 4.9 ± 0.14 (E1) and 4.3 ± 0.1 (E2), and the rest of the aftershock magnitudes (M_L) do not exceed 3.4. The stress drop estimated for E1 and E2 are 57 ± 7.4 and 28 ± 2.4 MPa, respectively, suggesting that the ruptures were associated with strong faults. These are capable of hosting earthquakes with long recurrence intervals, and our physics-based estimates of recurrence interval are 573 (E1) and 273 ka (E2). By analyzing the spatiotemporal distribution of earthquakes, we identify that the seismic sequence originated along a steep fault with a 218° strike, which then reactivated another sequence including E2 on a shallow-dipping fault with a 134° strike within 30 days of E1. Our Coulomb stress modeling indicate weak negative coupling between E1 and E2, precluding an explanation based on Coulomb stress transfer for fault interaction. Instead, we hypothesize that fault interaction was facilitated by fluid diffusion, local rotation of the stress field proceeding E1, or some combination of these processes. Interacting intraplate faults, with or without a prolonged time lag, have been observed previously in Australia (Jones et al., 1991; McCue, 1990), Asia (Liu et al., 2014; Liu et al., 2018), central and eastern United States (Li et al., 2005; Walsh et al., 2015), and in the Wharton basin beneath the Indian Ocean (Hill et al., 2015) following large earthquakes. Here we suggest that such fault interactions can take place even with moderate-sized earthquakes located several fault lengths apart. Also, an apparent correlation between heat flow and seismicity in southeast Australia suggests that intraplate seismicity is driven by a combination of mechanisms (e.g., transient stress perturbations, mechanical weakening from rifting and high heat flow). This understanding has important implications to the physics governing earthquakes and seismic hazard analysis.

Acknowledgments
The authors wish to acknowledge financial assistance provided through Australian National Low Emissions Coal Research and Development (ANLEC R&D) and the Education Investment Fund (EIF) for the project 7-1115-0284. ANLEC R&D is supported by Australian Coal Association Low Emissions Technology Limited and the Australian Government through the Clean Energy Initiative. Seismic monitoring equipment used in this study is part of AuScope's Australian Geophysical Observing System (AGOS) Subsurface Observatory and is funded through an Education Investment Fund (EIF) Round 3 grant. We acknowledge the many landowners who hosted temporary seismographs during this study and also thank the Seismology Research Centre (SRC) for providing data from private monitoring networks. Seismicity data in Figure 1 are obtained from IRIS Wilber 3. SAC (Goldstein et al., 2003), Taup Toolkit (Crotwell et al., 1999), and GMT5 (Wessel et al., 2013) were used for data processing and visualization. All data except those from the SR network can be accessed from the website (http://meiproc.earthsci.unimelb.edu.au/eqserver/). Access to SR data is restricted but can be obtained by contacting the authors. We also thank an anonymous reviewer, Takuji Yamada, and Editor Martha Savage for their comments that improved this manuscript significantly.

References

Abercrombie, R. E. (1995). Earthquake source scaling relationships from −1 to 5 M_L using seismograms recorded at 2.5 km depth. *Journal of Geophysical Research*, *100*(B12), 24,015–24,036. https://doi.org/10.1029/95JB02397

Aki, K., & Richards, P. G. (2009). *Quantitative seismology*, (2nd ed.p. 108). California: University Science Books.

Allen, T. I., Cummins, P., Dhu, T., & Schnieder, J. F. (2007). Attenuation of ground-motion spectral amplitudes in southeastern Australia. *Seismological Society of America*, *97*(4), 1279–1292. https://doi.org/10.1785/0120060172

Allmann, B. P., & Shearer, P. M. (2009). Global variations of stress drop for moderate to large earthquakes. *Journal of Geophysical Research*, *114*, B01310. https://doi.org/10.1029/2008JB005821

Anderson, E. M. (1905). The dynamics of faulting. *Transactions. Edinburgh Geological Society*, *8*(3), 387–402.

Attanayake, J., & Fonseca, J. F. B. D. (2016). The intraplate M_w 7 Machaze earthquake in Mozambique: Improved point source model, stress drop, and geodynamic implications. *Journal of African Earth Sciences*, *117*, 252–262. https://doi.org/10.1016/j.jafrearsci.2016.01.027

Baltay, A. S., Hanks, T. C., & Beroza, G. C. (2013). Stable stress-drop measurements and their variability: Implications for ground-motion prediction. *Bulletin of the Seismological Society of America*, *103*(1), 211–222. https://doi.org/10.1785/0120120161

Båth, M. (1965). Lateral inhomogeneities of the upper mantle. *Tectonophysics*, *2*(6), 483–514. https://doi.org/10.1016/0040-1951(65)90003-X

Bilham, R. (2014). Aggravated earthquake risk in South Asia: Engineering versus human nature. In M. Wyss (Ed.), *Earthquake hazard, risk, and disasters*, (pp. 103–141). Amsterdam: Elsevier. https://doi.org/10.1016/B978-0-12-394848-9.00005-5

Boatwright, J. (1978). Detailed spectral analysis of two small New York State earthquakes. *Bulletin of the Seismological Society of America*, *68*(4), 1117–1131.

Boatwright, J. (1980). A spectral theory for circular seismic sources; simple estimates of source dimension, dynamic stress drop, and radiated seismic energy. *Bulletin of the Seismological Society of America*, *70*(1), 1–27.

Bodin, P., & Horton, S. (2004). Source parameters and tectonic implications of aftershocks of the M_w 7.6 Bhuj earthquake of 26 January 2001. *Bulletin of the Seismological Society of America*, *94*(3), 818–827.

Bowman, J. R. (1992). The 1988 Tennant Creek, northern territory, earthquakes: A synthesis. *Australian Journal of Earth Sciences*, *39*(5), 651–669. https://doi.org/10.1080/08120099208728056

Brune, J. N. (1970). Tectonic stress and the spectra of seismic shear waves from earthquakes. *Journal of Geophysical Research*, *75*(26), 4997–5009. https://doi.org/10.1029/JB075i026p04997

Brune, J. N. (1986). Low stress-drop earthquakes in the light of new data from the ANZA, California telemetered digital array. In S. Das, J. Boatwright, & C. H. Scholz (Eds.), *Earthquake source mechanics*, *Geophysical Monograph Series* (Vol. 37, pp. 237–245). Washington, DC: American Geophysical Union. https://doi.org/10.1029/GM037

Bullen, K. E., & Bolt, B. A. (1985). *An introduction to the theory of seismology*, (pp. 188–190). Cambridge, UK: Cambridge University Press.

Calais, E., Camelbeeck, T., Stein, S., Liu, M., & Craig, T. J. (2016). A new paradigm for large earthquakes in stable continental plate interiors. *Geophysical Research Letters*, *43*, 10,621–10,637. https://doi.org/10.1002/2016GL070815

Calais, E., Mattioli, G., DeMets, C., Nocquet, J.-M., Stein, S., Newman, A., & Rydelek, P. (2005). Tectonic strain in plate interiors? *Nature*, *438*(7070), E9–E10. https://doi.org/10.1038/nature04428

Calais, E., & Stein, S. (2009). Time-variable deformation in the New Madrid Seismic Zone. *Science*, *323*(5920), 1442. https://doi.org/10.1126/science.1168122

Calligeros, M. (2014). Earthquakes in Victoria: The facts, the age. https://www.theage.com.au/national/victoria/earthquakes-in-victoria-the-facts-20141204-1201sk.html (last accessed on 24.08.2018).

Carvell, J., Blenkinsop, T., Clarke, G., & Tonelli, M. (2014). Scaling, kinematics and evo-lution of a polymodal fault system: Hail Creek Mine, NE Australia. *Tectonophysics*, *632*, 138–150. https://doi.org/10.1016/j.tecto.2014.06.003

Célérier, J., Sandiford, M., Hansen, D. L., & Quigley, M. (2005). Modes of active intraplate deformation, Flinders ranges, Australia. *Tectonics*, *24*, TC6006. https://doi.org/10.1029/2004TC001679

Chen, X., Shearer, P. M., & Abercrombie, R. E. (2012). Spatial migration of earthquakes within seismic clusters in Southern California: Evidence for fluid diffusion. *Journal of Geophysical Research*, *117*, B04301. https://doi.org/10.1029/2011JB008973

Clark, D., & McCue, K. (2003). Australian paleoseismology: Towards a better basis for seismic hazard estimation. *Annals of Geophysics*, *46*(N5), 1087–1105.

Clark, D., Mcpherson, A., & Allen, T. (2014). Intraplate earthquakes in Australia. In P. Talwani (Ed.), *Intraplate earthquakes*, (pp. 8–49). Cambridge: Cambridge University Press. https://doi.org/10.1017/CBO9781139628921.012

Clark, D., Mcpherson, A., & van Dissen, R. (2012). Long-term behaviour of Australian stable continental region (SCR) faults. *Tectonophysics*, *566-567*, 1–30. https://doi.org/10.1016/j.tecto.2012.07.004

Coblentz, D. D., Sandiford, M., Richardson, R. M., Zhou, S., & Hillis, R. (1995). The origins of the intraplate stress field in continental Australia. *Earth and Planetary Science Letters*, *133*(3–4), 299–309. https://doi.org/10.1016/0012-821X(95)00084-P

Coblentz, D. D., Zhou, S., Hillis, R., Richardson, R., & Sandiford, M. (1998). Topography, plate-boundary forces and the Indo-Australian intraplate stress field. *Journal of Geophysical Research*, *103*(B1), 919–931. https://doi.org/10.1029/97JB02381

Collins, C. D. N. (1988). Seismic velocities in the crust and upper mantle of Australia, Report 277, Bereau of Mineral Resources, Geology and Geophysics.

Copley, A., Hollingsworth, J., & Bergman, E. (2012). Constraints on fault and lithosphere rheology from the coseismic slip and postseismic afterslip of the 2006 M_w7.0 Mozambique earthquake. *Journal of Geophysical Research*, *117*, B03404. https://doi.org/10.1029/2011JB008580

Cotton, F., Archuleta, R., & Causse, M. (2013). What is sigma of the stress drop? *Seismological Research Letters*, *84*(1), 42–48. https://doi.org/10.1785/0220120087

Crone, A. J., de Martini, P. M., Machette, M. N., Okumura, K., & Prescott, J. R. (2003). Paleoseismicity of two historically quiescent faults in Australia: Implications for fault behavior in stable continental region. *Bulletin of the Seismological Society of America*, *93*(5), 1913–1934. https://doi.org/10.1785/0120000094

Crotwell, H. P., Owens, T. J., & Ritsema, J. (1999). The TauP ToolKit: Flexible seismic travel-time and raypath utilities. *Seismological Research Letters*, *70*(2), 154–160. https://doi.org/10.1785/gssrl.70.2.154

Davies, D. R., Rawlinson, N., Iaffaldano, N., & Campbell, I. H. (2015). Lithospheric controls on magma composition along Earth's longest continental hotspot track. *Nature*, *525*(7570), 511–514. https://doi.org/10.1038/nature14903

Dawson, J., Cummins, P., Tregoning, P., & Leonard, M. (2008). Shallow intraplate earthquakes in Western Australia observed by inter-ferometric synthetic aperture radar. *Journal of Geophysical Research*, *113*, B11408. https://doi.org/10.1029/2008JB005807

Dembo, N., Hamiel, Y., & Granot, R. (2015). Intraplate rotational deformation induced by faults. *Journal of Geophysical Research: Solid Earth*, *120*, 7308–7321. https://doi.org/10.1002/2015JB012264

Denham, D., Alexander, L. G., Everingham, I. B., Gregson, P. J., McCaffrey, R., & Enever, J. R. (1987). The 1979 Cadoux earthquake and intraplate stress in Western Australia. *Australian Journal of Earth Sciences*, *34*(4), 507–521. https://doi.org/10.1080/08120098708729429

Dentith, M. C., & Featherstone, W. E. (2003). Controld on intra-plate seismicity in southwestern Australia. *Tectonophysics*, *376*(3-4), 167–184. https://doi.org/10.1016/j.tecto.2003.10.002

Dickinson, J. A., Wallace, M. W., Holdgate, G. R., Gallagher, S. J., & Thomas, L. (2002). Origin and timing of the Miocene–Pliocene unconformity in southeast Australia. *Journal of Sedimentary Research*, *72*(2), 288–303. https://doi.org/10.1306/082701720288

Dieterich, J. H. (1972). Time-dependent friction in rocks. *Journal of Geophysical Research*, *77*(20), 3690–3697. https://doi.org/10.1029/JB077i020p03690

Dost, B., Edwards, B., & Bommer, J. J. (2018). The relationship between M and M_L: A review and application to induced seismicity in the Groningen Gas Field, the Netherlands. *Seismological Research Letters*, *89*(3), 1062–1074. https://doi.org/10.1785/02201700247

Dziewonski, A. M., Chou, T.-A., & Woodhouse, J. H. (1981). Determination of earthquake source parameters from waveform data for studies of global and regional seismicity. *Journal of Geophysical Research*, *86*(B4), 2825–2852. https://doi.org/10.1029/JB086iB04p02825

England, P., & Jackson, J. (2011). Uncharted seismic risk. *Nature Geoscience*, *4*(6), 348–349. https://doi.org/10.1038/ngeo1168

es&s (2010). eqFocus: User and installation manual for version 3.12 (revision 1), Environmental Systems and Services Pty. Ltd., http://www.src.com.au/wp-content/uploads/2014/01/eqFocus-User-Manual.pdf (last accessed 17.10.2018)

Eshelby, J. D. (1957). The determination of the elastic field of an ellipsoidal inclusion, and related problems. *Proceedings of the Royal Society of London. Series A: Mathematical and Physical Sciences*, *241*(1226), 376–396.

Etheridge, M. A., Branson, J. C., & Stuart-Smith, P. G. (1987). The Bass, Gippsland, and Otway basins, southeast Australia: A branched rift system formed by continental extension. In C. Beaumont, & A. J. Tankard (Eds.), *Sedimentary basins and basin-forming mechanisms*, *Canadian Society of Petroleum Geologists, Memoir* (Vol. 12, pp. 147–162).

Etheridge, M. A., McQueen, H. W. S., & Lambeck, K. (1991). The role of intraplate stress in Tertiary (and Mesozoic) deformation of the Australian continent and its margins: A key factor in petroleum trap formation. *Exploration Geophysics*, *22*, 123–128.

Fielding, C. R., Shaanan, U., & Rosenbaum, G. (2016). Sedimentological evidence for rotation of the early Permian Nambucca block (eastern Australia). *Lithosphere*, *8*(6), 684–698. https://doi.org/10.1130/L567.1

Forte, A. M., Mitrovica, J. X., Moucha, R., Simmons, N. A., & Grand, S. P. (2007). Descent of the ancient Farallon slab drives localized mantle flow below the New Madrid Seismic Zone. *Geophysical Research Letters*, *34*, L04308. https://doi.org/10.1029/2006GL027895

Gardner, T., Webb, J., Pezzia, C., Amborn, T., Tunnell, R., Flanagan, S., et al. (2009). Episodic intraplate deformation of stable continental margins: Evidence from late Neogene and Quaternary marine terraces, Cape Liptrap, southeastern Australia. *Quaternary Science Reviews*, *28*(1-2), 39–53. https://doi.org/10.1016/j.quascirev.2008.10.004

Gaull, B. A., Michael-Leiba, M. O., & Rynn, J. M. W. (1990). Probabilistic earthquake risk maps of Australia. *Australian Journal of Earth Sciences*, *37*(2), 169–187. https://doi.org/10.1080/08120099008727918

Gibson, G., Wesson, V., & Cuthbertson, R. (1981). Seismicity of Victoria to 1980. *Journal of the Geological Society of Australia*, *28*(3–4), 341–356. https://doi.org/10.1080/00167618108729173

Gitis, N. V., & Volpe, L. (1992). Nature of static friction time dependence. *Journal of Physics D: Applied Physics*, *25*(4), 605–612. https://doi.org/10.1088/0022-3727/25/4/006

Goebel, T. H. W., Becker, T. W., Schorlemmer, D., Stanchits, S., Sammis, C., Rybacki, E., & Dresen, G. (2012). Identifying fault heterogeneity through mapping spatial anomalies in acoustic emission statistics. *Journal of Geophysical Research*, *117*, B03310. https://doi.org/10.1029/2011JB008763

Goldstein, P., Dodge, D., Firpo, M., & Minner, L. (2003). SAC2000: Signal processing and analysis tools for seismologists and engineers. In W. H. K. Lee, H. Kanamori, P. C. Jennings, & C. Kisslinger (Eds.), *Invited contribution to the IASPEI international handbook of earthquake and engineering seismology*, (pp. 1613–1614). London: Academic Press.

Gomberg, J. S., Shedlock, K. M., & Roecker, S. W. (1990). The effect of *S*-wave arrival times on the accuracy of hypocentral estimation. *Bulletin of the Seismological Society of America*, *80*(6), 1605–1628.

Hardebeck, J. L., & Okada, T. (2018). Temporal stress changes caused by earthquakes: A review. *Journal of Geophysical Research: Solid Earth*, *123*, 1350–1365. https://doi.org/10.1002/2017JB014617

Hardebeck, J. L., & Shearer, P. M. (2002). A new method for determining first-motion focal mechanisms. *Bulletin of Seismological Society of America*, *92*(6), 2264–2276. https://doi.org/10.1785/0120010200

Hartzell, S. H., & Heaton, T. H. (1985). Teleseismic time functions for large shallow subduction zone earthquakes. *Bulletin of the Seismological Society of America*, *75*(4), 965–1004.

Havskov, J., & Ottemoller, L. (1999). SeisAn earthquake analysis software. *Seismological Research Letters*, *70*(5), 532–534. https://doi.org/10.1785/gssrl.70.5.532

Healy, D., Blenkinsop, T. G., Timms, N. E., Meredith, P. G., Mitchell, T. M., & Cooke, M. L. (2015). Polymodal faulting: Time for a new angle on shear failure. *Journal of Structural Geology*, *80*, 57–71. https://doi.org/10.1016/j.jsg.2015.08.013

Heidbach, O., Reinecker, J., Tingay, M., Müller, B., Sperner, B., Fuchs, K., & Wenzel, F. (2007). Plate boundary forces are not enough: Second- and third-order stress patterns highlighted in the world stress map database. *Tectonics*, *26*, TC6014. https://doi.org/10.1029/2007TC002133

Hill, E. M., Yue, H., Barbot, S., Lay, T., Tapponnier, P., Hermawan, I., et al. (2015). The 2012 M_w 8.6 Wharton Basin sequence: A cascade of great earthquakes generated by near-orthogonal, young, oceanic mantle faults. *Journal of Geophysical Research: Solid Earth*, *120*, 3723–3747. https://doi.org/10.1002/2014JB011703

Hiramatsu, Y., Yamanaka, H., Tadokoro, K., Nishigami, K., & Ohmi, S. (2002). Scaling law between corner frequency and seismic moment of microearthquakes: Is the breakdown of the cube law a nature of earthquakes? *Geophysical Research Letters*, *29*(8), 1211. https://doi.org/10.1029/2001GL013894

Holford, S. P., Hillis, R. R., Hand, M., & Sandiford, M. (2011). Thermal weakening localizes intraplate deformation along the southern Australian continental margin. *Earth and Planetary Science Letters*, *305*(1-2), 207–214. https://doi.org/10.1016/j.epsl.2011.02.056

Hough, S. E. (2014). Shaking from injection-induced earthquakes in the central and eastern United States. *Bulletin of the Seismological Society of America*, *104*(5), 2619–2626. https://doi.org/10.1785/0120140099

Houston, H., & Kanamori, H. (1986). Source spectra of great earthquakes: Teleseismic constraints on rupture process and strong ground motion. *Bulletin of the Seismological Society of America*, *76*(1), 19–42.

Huang, Y., Ellsworth, W. L., & Beroza, G. C. (2017). Stress drops of induced and tectonic earthquakes in the central United States are indistinguishable. *Science Advances*, *3*, e1700772.

Hummel, N., & Müller, T. M. (2009). Microseismic signatures of non-linear pore-fluid diffusion. *Geophysical Journal International*, *179*, 1558–1565. https://doi.org/10.1111/j.1365-246X.2009.04373.x

Johnston, A. C., & Kanter, L. R. (1990). Earthquake in stable continental crust. *Scientific American*, *262*(3), 42–49.

Jones, T. D., Gibson, G., McCue, K. F., Denham, D., Gregson, P. J., & Bowman, J. R. (1991). Three large intraplate earthquakes near Tennant Creek, Northern Territory, on 22 January 1988. *BMR Journal of Australian Geology and Geophysics*, *12*, 339–343.

Kanamori, H., & Allen, C. R. (1986). Earthquake repeat time and average stress drop. In S. Das, J. Boatwright, & C. H. Scholz (Eds.), *Earthquake source mechanics*, *Geophysical Monograph Series* (Vol. 37, pp. 227–235). Washington, DC: American Geophysical Union.

Kanamori, H., & Brodsky, E. E. (2004). The physics of earthquakes. *Reports on Progress in Physics*, *67*, 1429–1496.

Kaneko, Y., & Shearer, P. M. (2014). Seismic source spectra and estimated stress drop derived from cohesive-zone models of circular subshear rupture. *Geophysical Journal International*, *197*, 1002–1015.

Kazemian, J., Dominguez, R., Tiampo, K. F., & Klein, W. (2015). Spatial heterogeneity in earthquake-like systems. *Pure and Applied Geophysics*, *172*, 2167–2177. https://doi.org/10.1007/s00024-014-0843-6

Kenner, S. J., & Segall, P. (2000). A mechanical model for intraplate earthquakes: Application to the New Madrid Seismic Zone. *Science*, *289*, 2329–2332.

King, G. C. P., & Cocco, M. (2001). Fault interaction by elastic stress change: New clues from earthquake sequences. *Advances in Geophysics*, *44*, 1–38. https://doi.org/10.1016/S0065-2687(00)80006-0

King, G. C. P., Stein, R. S., & Lin, J. (1994). Static stress changes and the triggering of earthquakes. *Bulletin of the Seismological Society of America*, *84*(3), 935–953.

Krieger, L., & Heimann, S. (2012). MoPaD—Moment tensor plotting and decomposition: A tool for graphical analysis of seismic moment tensors. *Seismological Research Letters*, *83*(3), 589–595. https://doi.org/10.1785/gssrl.83.3.589
Leonard, M. (2008). One hundred years of earthquake recording in Australia. *Bulletin of the Seismological Society of America*, *98*, 1458–1470.
Leonard, M. (2010). Earthquake fault scaling: Relating rupture length, width, average displacement, and moment release. *Bulletin of the Seismological Society of America*, *100*, 1971–1988.
Leonard, M., Ripper, I. D., & Yue, L., (2002). Australian earthquake fault plane solutions, Record 2002/19, Geoscience Australia.
Levandowski, W., Herrmann, R. B., Briggs, R., Boyd, O., & Gold, R. (2018). An updated stress map of the continental United States reveals heterogeneous intraplate stresses. *Nature Geoscience*, *11*, 433–437.
Levenberg, K. (1944). A method for the solution of certain non-linear problems in least squares. *Quarterly of Applied Mathematics*, *2*, 164–168.
Li, Q., Liu, M., & Sandvol, E. (2005). Stress evolution following the 1811–1812 large earthquakes in the New Madrid Seismic Zone. *Geophysical Research Letters*, *32*, L11310. https://doi.org/10.1029/2004GL022133
Lienert, B. R. E., & Havskov, J. (1995). A computer program for locating earthquakes both locally and globally. *Seismological Research Letters*, *66*, 26–36.
Lin, J., & Stein, R. S. (2004). Stress triggering in thrust and subduction earthquakes and stress interaction between the southern San Andreas and nearby thrust and strike-slip faults. *Journal of Geophysical Research*, *109*, B02303. https://doi.org/10.1029/2003JB002607
Lin, Y.-Y., & Lapusta, N. (2018). Microseismicity simulated on asperity-like fault patches: On scaling of seismic moment with duration and seismological estimates of stress drops. *Geophysical Research Letters*, *45*, 8145–8155. https://doi.org/10.1029/2018GL078650
Liu, C., Dong, P., Zhu, B., & Shi, Y. (2018). Stress shadow on the southwest portion of the Longmen Shan fault impacted the 2008 Wenchuan earthquake rupture. *Journal of Geophysical Research: Solid Earth*, *123*, 9963–9981. https://doi.org/10.1029/2018JB015633
Liu, L., & Zoback, M. (1997). Lithospheric strength and intraplate seismicity in the New Madrid Seismic Zone. *Tectonics*, *16*(4), 585–595. https://doi.org/10.1029/97TC01467
Liu, M., & Stein, S. (2011). Aftershocks. In H. Gupta (Ed.), *Encyclopedia of solid earth geophysics* (pp. 192–194). Dordrecht, The Netherlands: Springer.
Liu, M., & Stein, S. (2016). Mid-continental earthquakes: Spatiotemporal occurences, causes, and hazards. *Earth-Science Reviews*, *162*, 364–386. https://doi.org/10.1016/j.earscirev.2016.09.016
Liu, M., Stein, S., & Wang, H. (2011). 2000 years of migrating earthquakes in North China: How earthquakes in midcontinents differe from those at plate boundaries. *Lithosphere*, *3*(2), 128–132. https://doi.org/10.1130/L129.1
Liu, M., Wang, H., Ye, J., & Jia, C. (2014). Intraplate earthquakes in north China. In P. Talwani (Ed.), *Intrplate earthquakes* (pp. 97–125). New York: Cambridge University Press.
Madariaga, R. (1976). Dynamics of an expanding circular fault. *Bulletin of the Seismological Society of America*, *66*(3), 639–666.
Marquardt, D. W. (1963). An algorithm for least-squares estimation of non-linear parameters. *Journal of the Society for Industrial and Applied Mathematics*, *11*(2), 431–441.
Mather, B., McLaren, S., Taylor, D., Roy, S., & Moresi, L. (2018). Variations and controld on crustal thermal regimes in southeastern Australia. *Tectonophysics*, *723*, 261–276. https://doi.org/10.1016/j.tecto.2017.12.015
McCue, K. (1990). Australia's large earthquakes and recent fault scarps. *Journal of Structural Geology*, *12*(5-6), 761–766.
Ming, Z., Hu, G., Jiang, X., Liu, S., & Yang, Y. (1995). *Catalog of Chinese historic strong earthquakes from 23 AD to 1911*, (p. 514). Beijing: Seismol. Press.
Montagner, J.-P., & Kennett, B. L. N. (1996). How to reconcile body-wave and normal-mode reference earth models. *Geophysical Journal International*, *125*, 229–248. https://doi.org/10.1111/j.1365-246X.1996.tb06548.x
Müller, D., Dyksterhuis, S., & Rey, P. (2012). Australian paleo-stress fields and tectonic reactivation over the past 100 Ma. *Australian Journal of Earth Sciences*, *59*(1), 13–28.
Nelson, E., Hillis, R., Sandiford, M., Reynolds, S., Lyon, P., Meyer, J., et al. (2006). Present-day state-of-stress of southeast Australia. *APPEA Journal*, *2006*, 283–305.
Oertel, G. (1965). The mechanism of faulting in clay experiments. *Tectonophysics*, *2*(5), 343–0393.
Oth, A., Miyake, H., & Bindi, D. (2017). On the relation of earthquake stress drop and ground motion variability. *Journal of Geophysical Research: Solid Earth*, *122*, 5474–5492. https://doi.org/10.1002/2017JB014026
Parsons, T., Malagnini, L., & Akinci, A. (2017). Nucleation speed limit on remote fluid-induced earthquakes. *Science Advances*, *3*(8), e1700660. https://doi.org/10.1126/sciadv.1700660
Prieto, G. A., Shearer, P. M., Vernon, F. L., & Kilb, D. (2004). Earthquake source scaling and self-similarity estimation from stacking *P* and *S* spectra. *Journal of Geophysical Research*, *109*, B08310. https://doi.org/10.1029/2004JB003084
Quigley, M., Clark, D., & Sandiford, M. (2010). Late Cenozoic tectonic geomorphology of Australia. *Geological Society of London*, *346*, 243–265.
Rajabi, M., Tingay, M., Heidbach, O., Hillis, R., & Renolds, S. (2017). The present-day stress field of Australia. *Earth-Science Reviews*, *168*, 165–189. https://doi.org/10.1016/j.earscirev.2017.04.003
Rawlinson, N., Pilia, S., Young, M., Salmon, M., & Yang, Y. (2016). Crust and upper mantle structure beneath southeast Australia from ambient noise and teleseismic tomography. *Tectonophysics*, *689*, 143–156. https://doi.org/10.1016/j.tecto.2015.11.034
Romanowicz, B., & Ruff, L. J. (2002). On the moment-length scaling of large strike-slip earthquakes and the strength of faults. *Geophysical Research Letters*, *29*(12), 1604. https://doi.org/10.1029/2001GL014479
Ron, H., & Beroza, G. (2001). Simple model explains complex faulting. *Eos, Transactions American Geophysical Union*, *82*(10), 125–132.
Sandiford, D. (2013). Seismo-tectonics in southeastern Australia: Insights from the Moe/Thropdale earthquakes, B.Sc. (Hons.) Thesis, University of Melbourne, Melbourne, Australia.
Sandiford, M. (2003). Neotectonics of southeastern Australia: Linking the Quaternary faulting record with seismicity and in situ stress. In R. R. Hillis, & D. Muller (Eds.), *Evolution and dynamics of the Australian Plate*, *Geological Society of Australia Special Publication* (Vol. 22, pp. 101–113).
Sandiford, M., & Egholm, D. L. (2008). Enhanced intraplate seismicity along continental margins: Some causes and consequences. *Tectonophysics*, *457*, 197–208. https://doi.org/10.1016/j.tecto.2008.06.004
Sandiford, M., & Quigley, M. (2009). TOPO-OZ: Insights into the various modes of intraplate deformation in the Australian continent. *Tectonophysics*, *474*, 405–416. https://doi.org/10.1016/j.tecto.2009.01.028
Sandiford, M., Wallace, M., & Coblentz, D. (2004). Origin of the in-situ stress field in southeastern Australia. *Basin Research*, *16*(3), 325–338.
Scholz, C. H., Aviles, C. A., & Wesnousky, S. G. (1986). Scaling differences between large interplate and intraplate earthquakes. *Bulletin of the Seismological Society of America*, *76*(1), 65–70.

Schulte, S. M., & Mooney, W. D. (2005). An updated global earthquake catalog for stable continental regions: Reassessing the correlation with ancient rifts. *Geophysical Journal International*, *161*, 707–721.
Shcherbakov, R., & Turcotte, D. L. (2004). A modified form of Båth's law. *Bulletin of the Seismological Society of America*, *94*(5), 1968–1975.
Shearer, P. M. (1999). *Introduction to seismology* (p. 114). Cambridge: Cambridge University Press.
Shearer, P. M. (2012). Self-similar earthquake triggering, Båth's law, and foreshock/aftershock magnitudes: Simulations, theory, and results for Southern California. *Journal of Geophysical Research*, *117*, B06310. https://doi.org/10.1029/2011JB008957
Sibson, R. H., & Xie, G. (1998). Dip range for intracontinental reverse fault ruptures: Truth not stranger than friction? *Bulletin of the Seismological Society of America*, *88*(4), 1014–1022.
Smith, W. H. F., & Wessel, P. (1990). Gridding with continuous curvature splines in tension. *Geophysics*, *55*, 293–305.
Stein, C. A., Stein, S., Merino, M., Randy Keller, G., Flesch, L. M., & Jurdy, D. M. (2014). Was the Midcontinent Rift part of a successful seafloor-spreading episode? *Geophysical Research Letters*, *41*, 1465–1470. https://doi.org/10.1002/2013GL059176
Stein, R. (1999). The role of stress transfer in earthquake occurrence. *Nature*, *402*, 605–609.
Stein, R. S., Barka, A. A., & Dieterich, J. H. (1997). Progressive failure on the North Anatolian fault since 1939 by earthquake stress triggering. *Geophysical Journal International*, *128*(3), 594–604. https://doi.org/10.1111/j.1365-246X.1997.tb05321.x
Stein, S., & Liu, M. (2009). Long aftershock sequences within continents and implications for earthquake hazard assessment. *Nature*, *462*, 87–89. https://doi.org/10.1038/nature08502
Stephansson, O., Ljunggren, C., & Jing, L. (1991). Stress measurements and tectonic implications for Fennoscandia. *Tectonophysics*, *189*, 317–322.
Stork, A. L., Verdon, J. P., & Kendall, J.-M. (2014). The robustness of seismic moment and magnitudes estimated using spectral analysis. *Geophysical Prospecting*, *62*, 862–878. https://doi.org/10.1111/1365-2478.12134
Talwani, P. (2014). Unified model for intraplate earthquakes. In P. Talwani (Ed.), *Intraplate earthquakes*, (pp. 275–302). Cambridge: Cambridge University Press. https://doi.org/10.1017/CBO9781139628921.012
Talwani, P., Chen, L., & Gahalaut, K. (2007). Seismogenic permeability, k_s. *Journal of Geophysical Research*, *112*, B07309. https://doi.org/10.1029/2006JB004665
Talwani, P., & Rajendran, K. (1991). Some seismological and geometric features of intraplate earthquakes. *Tectonophysics*, *186*, 19–41.
Tarayoun, A., Mazzotti, S., Craymer, M., & Henton, J. (2018). Structural inheritance control on intraplate present-day deformation: GPS strain rate variations in the Saint Lawrence Valley, eastern Canada. *Journal of Geophysical Research: Solid Earth*, *123*, 7004–7020. https://doi.org/10.1029/2017JB015417
Toda, S., Stein, R. S., Richards-Dinger, K., & Bozkurt, S. B. (2005). Forecasting the evolution of seismicity in southern California: Animations built on earthquake stress transfer. *Journal of Geophysical Research*, *110*, B05S16. https://doi.org/10.1029/2004JB003415
Vandenberg, A. H. M. (2010). Paleogene basalts prove early uplift of Victoria's eastern uplands. *Australian Journal of Earth Sciences*, *57*(3), 291–315. https://doi.org/10.1080/08120091003619225
Waldhauser, F., & Ellsworth, W. L. (2000). A double-difference earthquake location algorithm: Method and application to the northern Hayward fault. *Bulletin of the Seismological Society of America*, *90*, 1353–1368.
Walsh, L. S., Montési, L., & Martin, A. J. (2015). Coulomb stress transfer and modeled permanent vertical surface deformation from the August 2011, Mineral, Virginia, earthquake. In J. W. Horton, M. C. Chapman, & R. A. Green (Eds.), *The 2011 Mineral, Virginia, Earthquake, and its significance for seismic hazards in eastern North America*, *Geol. Soc. Am. Special Paper* (Vol. 509, pp. 305–329).
Ward, S. N. (1998). On the consistency of earthquake moment rates, geological fault data, and space geodetic strain: The United States. *Geophysical Journal International*, *134*, 172–186.
Wessel, P., Smith, W. H. F., Scharroo, R., Luis, J., & Wobbe, F. (2013). Generic mapping tools: Improved version released. *Eos, Transactions American Geophysical Union*, *94*(45), 409–410. https://doi.org/10.1002/2013EO450001
Wesson, V. C. (1988). Seismic modeling of the Victorian lithosphere, Masters Thesis, Philip Institute of Technology, Melbourne.
Wills, S., & Buck, W. R. (1997). Stress-field rotation and rooted detachment faults: A Coulomb failure analysis. *Journal of Geophysical Research*, *102*(B9), 20,503–20,514. https://doi.org/10.1029/97JB01512
Wolin, E., Stein, S., Pazzaglia, F., Meltzer, A., Kafka, A., & Berti, C. (2012). Mineral, Virginia, earthquake illustrates seismicity of a passive-aggressive margin. *Geophysical Research Letters*, *39*, L02305. https://doi.org/10.1029/2011GL050310
Yamada, T., Yukutake, Y., Terakawa, T., & Arai, R. (2015). Migration of earthquakes with a small stress drop in the Tanzawa Mountains, Japan. *Earth, Planets and Space*, *67*, 175. https://doi.org/10.1186/s40623-015-0344-6
Yin, Z. M., & Rogers, G. C. (1995). Rotation of the principal stress directions due to earthquake faulting and its seismological implications. *Bulletin of the Seismological Society of America*, *85*(5), 1513–1517.
Yoshida, K., & Hasegawa, A. (2018). Hypocenter migration and seismicity pattern change in the Yamagata- Fukushima border, NE Japan, caused by fluid movement and pore pressure variation. *Journal of Geophysical Research: Solid Earth*, *123*, 5000–5017. https://doi.org/10.1029/2018JB015468
Yukutake, Y., Ito, H., Honda, R., Harada, M., Tanada, T., & Yoshida, A. (2011). Fluid-induced swarm earthquake sequence revealed by precisely determined hypocenters and focal mechanisms in the 2009 activity at Hakone volcano, Japan. *Journal of Geophysical Research*, *116*, B04308. https://doi.org/10.1029/2010JB008036
Zhao, S., & Müller, R. D. (2001). The tectonic stress field in Eastern Australia, PESA Eastern Australian Basins Symposium, Melbourne, Vic, 25–28 November, 2001.
Zielke, O., Galis, M., & Mai, P. M. (2017). Fault roughness and strength heterogeneity control earthquake size and stress drop. *Geophysical Research Letters*, *44*, 777–783. https://doi.org/10.1002/2016GL071700
Zoback, M. L. (1992). Stress field constraints on intraplate seismicity in eastern North America. *Journal of Geophysical Research*, *97*(B8), 11,761–11,782. https://doi.org/10.1029/92JB00221

References From the Supporting Information

Vandenberg, A. H. M. (1997). Warragul SJ 55-10 Edition 2, 1:250 000 Geological Map Series. 1:250 000 geological map. Geological Survey of Victoria.